DIGIT: *Herschel*[⋆] and *Spitzer* spectro-imaging of SMM3 and SMM4 in Serpens

O. Dionatos[1,2,3], J. K. Jørgensen[2,1], J. D. Green[4], G. J. Herczeg[5], N. J. Evans II[4], L. E. Kristensen[6], J. E. Lindberg[1,2], and E. F. van Dishoeck[6,7]

[1] Centre for Star and Planet Formation, Natural History Museum of Denmark, University of Copenhagen, Øster Voldgade 5 – 7, DK-1350 Copenhagen K. Denmark
e-mail: odysseas@nbi.ku.dk

[2] Niels Bohr Institute, University of Copenhagen. Juliane Maries Vej 30, DK-2100 Copenhagen Ø. Denmark

[3] University of Vienna, Department of Astronomy, Türkenschanzstrasse 17, A-1180, Vienna, Austria

[4] University of Texas at Austin, Department of Astronomy, 2515 Speedway, Stop C1400, Austin, TX 78712-1205, USA

[5] Kavli Institute for Astronomy and Astrophysics, Peking University, Beijing, 100871, PR China

[6] Leiden Observatory, Leiden University, P.O. Box 9513, NL-2300 RA Leiden, The Netherlands

[7] Max Planck Institut für Extraterrestrische Physik, Giessenbachstrasse, D-85748 Garching, Germany

ABSTRACT

Context. Mid- and far-infrared observations of the environment around embedded protostars reveal a plethora of high excitation molecular and atomic emission lines. Different mechanisms for the origin of these lines have been proposed, including shocks induced by protostellar jets, and radiation or heating by the embedded protostar of its immediate surroundings.

Aims. Through the study of the most important molecular and atomic coolants, we aim at constraining the physical conditions around two protostars in the Serpens molecular cloud core and measuring the CO/H_2 ratio in warm gas.

Methods. We employ spectro-imaging observations from Spitzer/IRS and Herschel/PACS providing an almost complete wavelength coverage between 5 and 200 μm to observe the environment around the embedded protostars SMM3 and SMM4 in Serpens. Within this range, emission from all major molecular (H_2, CO, H_2O and OH) and many atomic ([OI], [CII], [FeII], [SiII] and [SI]) coolants of excited gas are detected.

Results. Line emission tends to peak at distances of $\sim$10–20″ from the protostellar sources, with all but [CII] peaking at the positions of outflow shocks seen in near-IR and sub-millimeter interferometric observations. Excitation analysis indicates that H_2 and CO originate from gas at two distinct rotational temperatures of $\sim$300 K and 1000 K, while the excitation temperature for H_2O and OH is $\sim$100–200 K. The morphological and physical association between CO and H_2 suggests a common excitation mechanism which allows direct comparisons between the two molecules. The CO/H_2 abundance ratio varies from $\sim 10^{-5}$ in the warmer gas up to $\sim 10^{-4}$ in the hotter regions. The existence of J-shocks is suggested by the strong atomic/ionic (except for [CII]) emission as well as a number of line ratio diagnostics. Dissociative shocks can account for the CO and H_2 emission in a single excitation temperature structure.

Conclusions. The bulk of cooling from molecular and atomic lines is associated with gas excited in outflow shocks. The strong association between H_2 and CO enable to constrain their abundance ratio in warm gas, which is found to vary between 10^{-4} and 10^{-5}. Both C- and J-type shocks can account for the observed molecular emission, however J-shocks are strongly advocated by the atomic emission and provide simpler and more homogeneous solutions for CO, H_2. The variations in the CO/H_2 abundance ratio for gas at different temperatures can be interpreted by their reformation rates in dissociative J-type shocks, or the influence of both C and J shocks

Key words. stars: formation - infrared - sub-mm lines: ISM - ISM: jets and outflows - molecular processes - shock waves

1. Introduction

Protostellar outflows moving at supersonic velocities interact with the interstellar medium through shocks. Such interactions result in heating, compressing and setting the gas into motion.

On large, outflow scales, varying physical conditions may occur due to the intrinsic physical properties of the underlying primary protostellar jet and the way it propagates (e.g. Arce et al. 2007). On scales of individual shocks, the physics depends mainly on the energy transfer and the possible presence of magnetic fields (e.g. Hollenbach & McKee 1989). The combined effect of these mechanisms produce physical and chemical gradients along the outflows on all spatial scales. Shock-excited gas cools mainly

---

[⋆] *Herschel* is an ESA space observatory with science instruments provided by European-led Principal Investigator consortia and with important participation from NASA.

through atomic and molecular line radiation, e.g., near- and mid-infrared H_2 transitions (corresponding to temperatures of a few thousand K) and far-infrared lines of CO and H_2O (temperatures from a few hundred up to ~ 1000 K). Swept-up ambient material with temperatures of a few tens of K is commonly traced by low energy CO transitions, falling in the (sub)millimeter regime (Arce et al. 2007). A complete census connecting these two regimes is required for understanding the physical mechanisms relating the shocks to the large-scale outflows and the energy transfer from the vicinity of the protostar to the surrounding medium, including the cooling taking place at the intermediate energies.

The ISO satellite (Kessler et al. 1996) made important contributions bridging the two energy regimes (e.g. van Dishoeck 2004). Observations with the SWS, LWS and CVF instruments revealed many molecular (H_2, CO, H_2O, OH) and atomic ([OI], [CII]) lines, which have helped to understand the shock cooling in protostellar outflows (Giannini et al. 2001). The angular resolution of ISO, however, was only sufficient to study the cumulative effect of different processes within its beam of $\sim 80''$ (LWS) and understanding the outflow physics therefore had to rely on in-depth modeling (e.g. Nisini et al. 2000; Giannini et al. 2006).

Observations of protostellar outflows with the Spitzer Space Telescope (Werner et al. 2004) and more recently the Herschel Space Observatory (Pilbratt et al. 2010) have provided us a more detailed view of the physical processes along outflows, through spectral images with angular resolutions ranging between 3.5″ and 9.4″ (for the IRS and PACS instruments, respectively). Spectro-imaging is a powerful tool for the study of extended emission structures, permitting us to retrieve simultaneously the spatial distribution and spectral information of an excited region. This allows to disentangle the contribution of UV-heated outflow cavities from emission due to shocks along the outflow propagation axis (e.g. Visser et al. 2012; Herczeg et al. 2012; van Kempen et al. 2010). The spatial distribution of isolated spectral features provides morphological evidence for the origin of the excited gas, whereas the study of the spectral information provides information on the underlying physical conditions (e.g. Kristensen et al. 2010b). In the mid-IR, "synthetic" (i.e. reconstructed from slit-scan observations) spectral maps have been obtained with the Spitzer/IRS spectrograph for a number of individual protostars (Neufeld et al. 2006, 2009; Dionatos et al. 2010a; Nisini et al. 2010) and star-forming regions (Maret et al. 2009). PACS onboard Herschel comes with built-in spectro-imaging capabilities at angular resolutions comparable to Spitzer/IRS. We here employ spectral maps from both instruments to study the excitation of the medium around the embedded protostars in the Serpens star forming region.

Since its first identification as an active star-forming region by Strom et al. (1976), the Serpens cloud core has attracted much attention owing to its remarkably high stellar density and star formation efficiency (e.g. Enoch et al. 2007) observed within its limited extent of a few arc-minutes ($\sim$0.2-0.4 pc for the distance estimates ranging between 260 pc (Straižys et al. 2003) and 415±25 pc (Dzib et al. 2010), the latter adopted in this work). Among the stellar population of the Serpens complex, ~ 30 embedded (Class 0 & I) protostars have been identified (Winston et al. 2007; Harvey et al. 2007), distributed within two main clumps at the northwest and southeast, as opposed to a dispersed population of more evolved (Class II) protostars along the cluster. The continuum and line emission from embedded sources in Serpens has been studied with ISO/LWS and CVF instruments (Larsson et al. 2000, 2002). Nevertheless, the limited spatial resolution ($\sim 80''$) of the LWS was not sufficient to con-
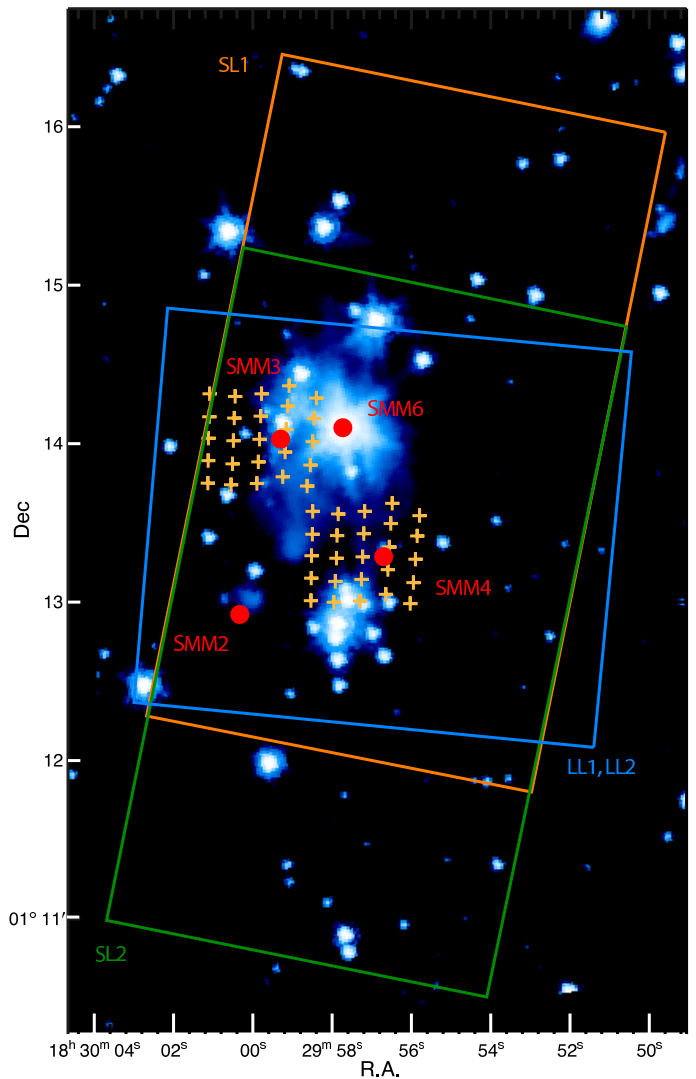

Fig. 1. Regions of the Serpens SE cluster observed with Spitzer/IRS and Herschel/PACS superimposed on a Spitzer IRAC 4.5 μm image. Dark orange, green and blue rectangles correspond to the areas mapped with Spitzer/IRS modules SL1, SL2 and LL1/LL2, respectively. Orange crosses denote the 5×5 Herschel/PACS footprints around the protostellar sources SMM3 and SMM4. Positions of known embedded sources in the region are indicated with filled red circles.

strain and differentiate the possible mechanisms responsible for the excitation of the gas. In addition, the available spectral resolution (R$\sim$ 200) and sensitivity allowed only the detection of the strongest, often blended, emission lines.

Here we present combined spectro-imaging observations of the embedded protostars SMM3 and SMM4, located in the SE region in Serpens with Spitzer/IRS and Herschel PACS. The combined power of both instruments provides an almost complete wavelength coverage between 5 and 200 μm. These observations cover almost the same wavelength regime as the ISO observations presented in Larsson et al. (2002) ($\sim$ 5-190 μm) at an average angular resolution of $\sim$9.4″ and at spectral resolutions ranging from R=60-120 (IRS) to R=1500-3000 (PACS). Compared with ISO observations, Herschel/PACS provides an improvement by a factor of $\sim$5 in angular and $\sim$10 in spectral resolution.

The paper is organized as follows: Sect. 2 presents the observations and describes the reduction of the data. Sect. 3 discusses the emission morphology revealed by line and continuum maps around SMM3 and SMM4. The underlying excitation conditions are derived with analytical methods and further discussed in comparison to shock models in Sect. 4. Finally, Sect. 5 puts into context the main results from the analysis and Sect. 6 provides a summary of this work.

2. Observations and data reduction

2.1. Herschel/PACS

Observations were obtained with the Photodetector Array Camera and Spectrometer (PACS; Poglitsch et al. 2010) as part of the "Dust, Ice and Gas in Time (DIGIT)" open time key-project (Green et al. 2013). PACS is a 5×5 array of 9.4″×9.4″ spatial pixels (referred to as spaxels). The spectral range extends from 51 to 210 μm with R ~ 1000–3000, divided into four segments, covering λ ~ 50–75, 70–105, 100–145, and 140–210 μm. The half power beam size of Herschel ranges from ~5″ at 50 μm to ~13″ at 200 μm and therefore the nominal spaxel size of PACS (9.4″) is a compromise between these two limits.

Observations were performed in range-scan spectroscopy mode, providing the complete coverage of the wavelength range observable by PACS. Two footprints were observed targeting the protostellar sources SMM3 (α_{J2000}= $18^h29^m59^s.3$, δ_{J2000}=+$01^d14^m01^m.7$) and SMM4 (α_{J2000}=$18^h29^m56^s.7$, δ_{J2000}=+$01^d13^m17^m.2$), as reported in Harvey et al. (2007). Both sources were observed on April 2nd, 2010 with an integration time for each footprint of 4.2 hours. The telescope and sky background emission was subtracted using two nod positions 6′ from the source in opposite directions. The observations were done in single staring mode, that is the obtained maps are not Nyquist sampled. For both sources observations were mispointed by ~7″ to the west, as presented in Fig. 1. This offset is attributed to the instrument pointing calibration accuracy during the first phases of the mission, which exhibited residuals of this magnitude (see the Herschel Pointing Calibration Report, v1.0 - HERSCHEL-HSC-DOC-1515). The pointing offset has been accounted for in all comparisons to other data in the following sections.

The data were reduced following the general procedure adopted for the DIGIT embedded objects, described in detail in Green et al. (2013). Summarizing, the reduction pipelines provide us with two data products which are based on HIPE versions 6.1 and 8.0, respectively. For the first data product (DP1) we employ the telescope background calibration method (HIPE 6.1) which results in best continuum matches between the different spectral segments. In addition, absolute flux calibration is found to be good to a 10% level when compared to Spitzer and Herschel photometry (see Fig. 2). The second data product (DP2) is based on the calibration block method (HIPE 8.0) and provides a better signal-to-noise ratio (SNR) on individual lines. In this dataset however the overall continuum fluxes are not well calibrated and spectral segments show discontinuous jumps. The continuum and line fluxes between the two datasets scale by the same factor, which varies with wavelength. Therefore the flux calibrations in DP2 are affected by a multiplicative calibration error. Representative DP2 spectra (Fig. 3) display a significant number of lines from CO, H_2O, OH, [OI] and [CII]. Spectra in the blue segments (<100 μm) have an average noise level of ~ 0.25 Jy, more than double compared to the ~ 0.1 Jy in the red
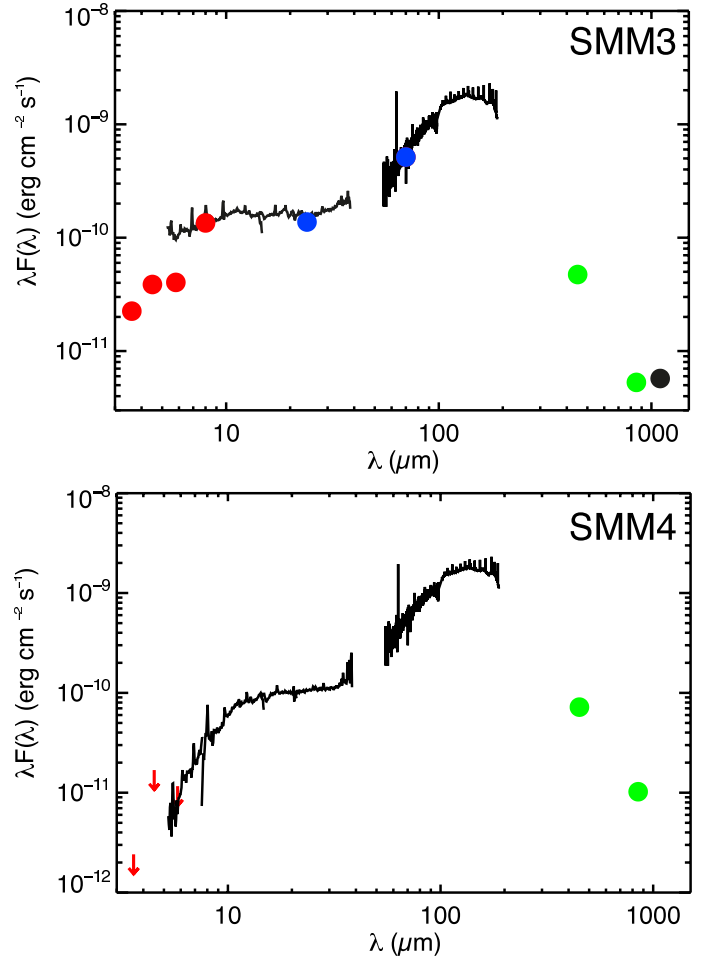

Fig. 2. Spectral energy distribution diagram of SMM3 and SMM4 (upper and lower panels, respectively) along with spectra from Spitzer/IRS and Herschel/PACS. Fluxes for both instruments are extracted within a region encompassing the 3x3 central spaxels of PACS. Filled circles are flux densities from IRAC at 3.6, 4.5. 5.8 and 8.0 μm bands (red, Harvey et al. 2007), MIPS at 24 and 70 μm (blue, Harvey et al. 2007), SCUBA at 450 and 850 μm, (green, Davis et al. 1999) and 1100 μm (black, Enoch et al. 2007). Red arrows represent upper limit values for the IRAC bands.

modules. No other lines were identified after thorough comparisons against molecular and atomic line catalogues.

Line fluxes were determined for each individual spaxel. They were initially calculated in DP2 by fitting the line profile with a gaussian, after having subtracted a first order polynomial baseline. Subsequently, line fluxes were scaled to match DP1 levels providing the correct flux levels. Additional corrections for flux spillover were applied by scaling the line fluxes with the instrumental PSF. This assumes that most of the emission arises from selected individual spaxels and the spill over between these spaxels is not significant. Disentangling the origin of extended emission can be complex (see Sect. 3.1.4) and PSF corrections may underestimate the total emission from a single spaxel (Karska et al. 2013). Spectra in the range between 96 and 103 μm are exceedingly noisy and show irregular variations in the the continuum flux levels. Abnormally low flux levels are also evident beyond 190 μm along with "ghost" spectral features due to leakage of emission from higher orders. Therefore line fluxes from these two parts are unreliable and have been excluded.
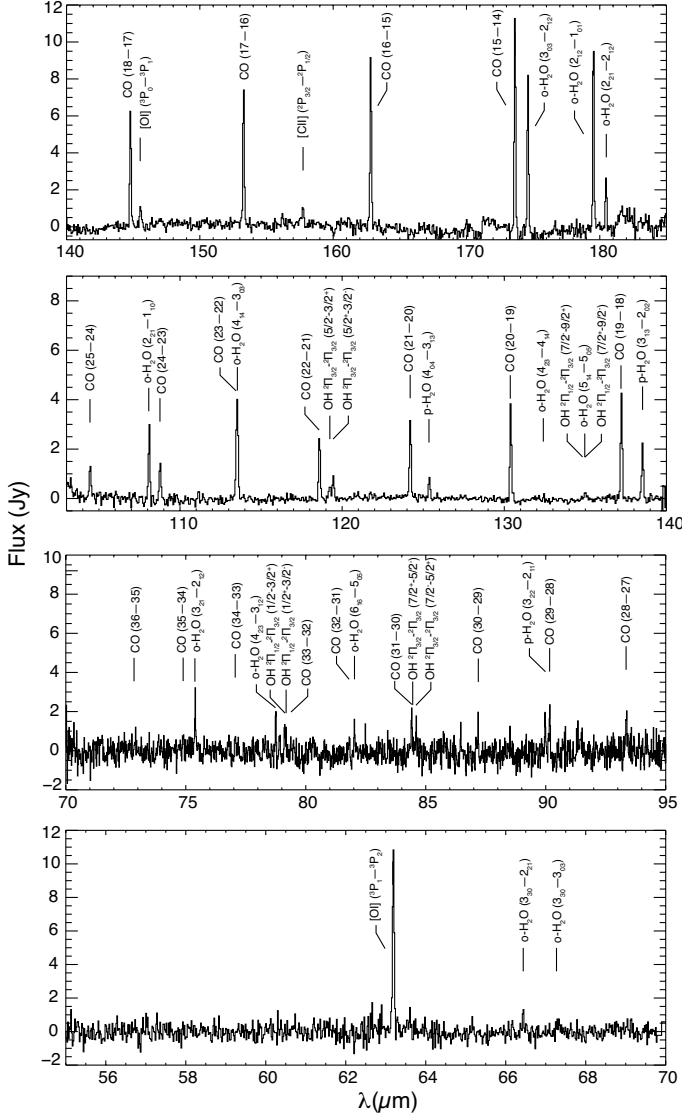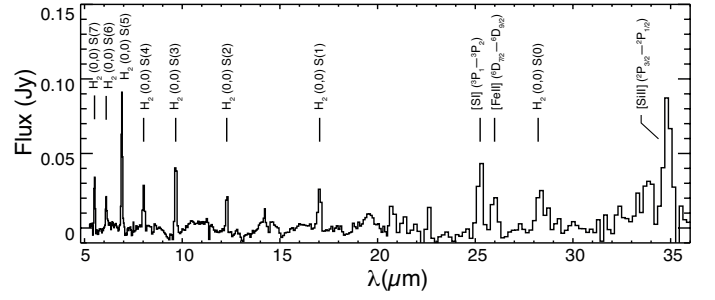
Fig. 4. IRS spectrum extracted at the PACS spatial scale encompassing the same region as the PACS spectrum in fig 3. Molecular (H_2) and forbidden atomic transitions ([SI], [FeII], [SiII]) are marked on top of each line detected. Unidentified line-like features are due to residual bad/rogue pixels

Integration times per pointing were 28 and 60 seconds for the SL and LL modules, respectively.

Initial data processing was performed with version S18.7 of the *Spitzer* Science Center pipeline. Spectral data cubes were compiled using the CUBISM software (Smith et al. 2007), and bad/rogue pixels were masked by visual inspection. As in the case of PACS, emission line maps were constructed through customized procedures. In these, for each spaxel of a data-cube, the flux for each spectral line of interest was calculated by fitting a Gaussian after subtracting a local first or second order polynomial baseline. The resulting line intensity maps for the IRS data have a square spaxel of side equal to the width of the low resolution IRS modules (3.5″ and 10.5″ for the SL and LL modules, respectively), while the half power beam size of Spitzer ranges between 3″ at 5.2 μm to 10″ at 38 μm. Full resolution line maps are presented in Fig. 14 and in appendix A. For direct comparison with the PACS maps, IRS data cubes were resampled according to the Herschel pointings at the PACS spaxel size of 9.4″, therefore providing analogous spectral line maps. The maximum half power beam size of Spitzer is comparable to the PACS spaxel dimensions, and therefore no significant flux losses are expected to occur after resampling the IRS maps to the PACS grid. A resampled spectrum encompassing the same area as PACS in Fig. 1 towards the outflow of SMM3 is shown in Fig 4; strong emission lines from the first eight pure rotational transitions of hydrogen (S(0) - S(7)), as well as atomic and ionic lines from [FeII], [SI] and [SiII] are seen, indicating along with the PACS spectra highly energetic conditions.

3. Spectral maps

3.1. Herschel

3.1.1. Continuum emission

Figure 5 presents maps of the PACS continuum levels at 80, 130 and 180 μm (red contours, running from left to right) around SMM3 and SMM4 overlaid on top of a Spitzer/MIPS 70 μm image. In the same figure, green contours shape the 450 μm continuum emission observed with SCUBA (Davis et al. 1999), while the filled yellow and red dots display the positions of SMM3 and SMM4 derived from Spitzer (Harvey et al. 2007) and millimeter interferometric observations (at λ =3.4, 3.2, 2.7 and 1.4 mm, Hogerheijde et al. 1999). PACS continuum emission at 80 μm follows well the brightness distribution of the 70 μm underlying image, showing peaks to the west of SMM3 and both to the NE and SE of SMM4. In the 130 μm and 180 μm maps, the con-

Fig. 3. PACS continuum-subtracted spectrum from a single spaxel at the NW of SMM3. Molecular and atomic transitions are reported on top of each detected line.

2.2. Spitzer/IRS

Spitzer observations were retrieved from the Spitzer Heritage Archive (SHA)[1]. They have been performed as part of the c2d program (Evans et al. 2003, 2009; Lahuis et al. 2010). In these data, the low resolution (R ~ 60 - 120) modules short-low (SL) and long-low (LL) of the Spitzer Infrared Spectrograph (IRS, Houck et al. 2004) were employed, providing a complete wavelength coverage between 5.2 and 38.0 μm. Observations were performed in slit-scan mode consisting of consecutive integrations after shifting the slit to the parallel and perpendicular directions in relation to the slit length, until the desired area is covered. The SL scans consist of 5 × 43 such observations, where the SL slit was offset by 3.5″ in the parallel and 50″ in the perpendicular directions, covering a total area of 145″×255″. Similarly, the LL scans consist of 1x15 observations, offsetting the LL slit by 9.5″ only in the parallel direction (Fig. 1).

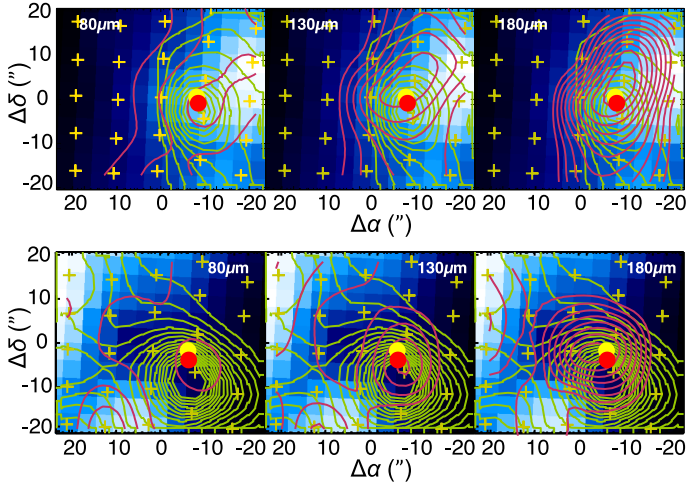[1] http://sha.ipac.caltech.edu/applications/Spitzer/SHA/

4

Fig. 5. PACS continuum levels at 80, 130 and 180 μm (red contours) superimposed on a Spitzer/MIPS 70 μm images around SMM3 and SMM4 (upper and lower panels, respectively). Green contours show the 450 μm continuum observed with SCUBA, while the yellow and red dots depict the position of the sources reported in Harvey et al. (2007) and Hogerheijde et al. (1999). PACS and SCUBA levels start at 2 Jy and increase by 2 Jy and 1.5 Jy steps, respectively.

tinuum morphology gradually departs from the MIPS brightness profile with the observed peaks shifting closer to the nominal source positions. The distribution of warm dust detected here is not symmetric around the protostellar sources, indicating asymmetric envelope morphologies and substantial continuum emission in the direction of outflows. The emission at the longest continuum wavelength (180 μm) from PACS does not overlap completely with the SCUBA data at 450 μm, suggesting at peak farther south in column density than is apparent in the PACS maps.

3.1.2. Molecular emission

Figure 6 presents integrated line emission maps of the CO transitions detected with PACS around SMM3. CO emission is extended, exceeding the dimensions of the PACS footprint in the N-S direction except for the transitions with $J_{up} \geq 34$ where it shows a single peak. The emission pattern runs roughly in the NNW-SSE direction, and strongly peaks towards the NW from the center, at a distance of $\sim 20''$. At roughly the same distance from the center, a secondary peak becomes apparent for intermediate J transitions ($24 < J_{up} < 31$) towards the southern edge of the map. At higher energy transitions, emission becomes weaker and the emission pattern less clear.

Maps of the CO lines detected with PACS around SMM4 are presented in Fig. 7. The line emission pattern is more centralized than in the case of SMM3, and peaks off the central spaxel and to the north of the protostellar source at a distance of $\sim 5''$. Similarly to SMM3, emission becomes weaker with increasing J showing only local maxima for $J_{up} \geq 32$. Therefore the high-J and mid-J CO lines do not necessarily co-exist in all positions.

Figs. 8 and 9 present the strongest water lines around SMM3 and SMM4 traced by PACS. For both sources, the observed morphologies are very similar to the CO maps, with the only exception being a secondary peak observed towards the southern lobe of SMM3 at $\sim 10''$ from the center, in a similar fashion to the high-J CO lines. This difference in the emission pattern

of the two molecules may reflect differences in their excitation (see Sect. 4). H_2O line emission maps display a decline in intensity moving from lower to higher excitation energy transitions, which eventually is concentrated around the spaxels showing emission maxima.

OH doublets at 71.2 and 79.1 μm are not spectrally resolved at the signal-to-noise ratio in the blue segments, and resolved doublets at 84.4 and 134.8 μm are blended with much stronger CO and H_2O lines (see Table 1). OH emission (Fig. 10) is in general weak and lines are detected in most cases at the spaxels where CO and H_2O peak, with the single exception of the OH ($^2\Pi_{\frac{3}{2}} - ^2\Pi_{\frac{3}{2}}$, $J = \frac{5}{2}^- - \frac{3}{2}^+$) line at 119.2 μm which appears to follow the extended emission pattern traced by CO and H_2O.

The molecular emission morphology can provide indications of the underlying processes responsible for the excitation of the gas. Despite small differences, CO, H_2O and OH trace similar or related morphologies seen in each source. However, the pattern observed around SMM3 is substantially different from that seen around SMM4. Emission around the former source is in all cases extended, whereas in the latter case, lines peak off the protostellar source, but the emission pattern is more compact. In both cases, emission peaks offset from the sources, but the extent and symmetry of the observed structures present no further resemblance.

Observations of high velocity emission from low energy levels of CO, such as $J = 3-2$ (Dionatos et al. 2010b; Graves et al. 2010) and see Fig. 11, and $J = 2-1$, (Davis et al. 1999), at resolutions $\sim 7''-15''$, comparable to those provided by PACS, show very similar structures which are attributed for both sources to outflows. In the case of SMM3, the NNW and SSE lobes appear to be blue- and red-shifted, respectively, whereas in the case of SMM4, the emission structure coincides with blue-shifted gas. A red-shifted lobe to the SE, often attributed to SMM4 (e.g. Narayanan et al. 2002; Dionatos et al. 2010b) is not traced here by PACS.

Around both SMM3 and SMM4, shock excited H_2 emission following the outflow pattern has been recorded in the near and mid-IR (e.g. Herbst et al. 1997; Eiroa et al. 1997; Larsson et al. 2002, see also the following section 3.2). Similar outflows are recorded in the methanol maps of Kristensen et al. (2010a). High resolution maps in several molecular lines, such as HCO^+, HCN, SiO (Hogerheijde et al. 1999) and CS (Testi et al. 2000) reveal narrow, jet-like structures following the outflow orientations.

3.1.3. Atomic emission

Line maps of atomic species observed with PACS around SMM3 and SMM4 are presented in Fig. 12 (upper and lower panels, respectively). The emission pattern for the [OI] line at 63.2 and 145 μm around both sources is similar, given the lower signal-to-noise and resolution of the latter line. Both lines follow the pattern delineated by the molecular tracers and peak at the same positions.

The [CII] emission line maps reveal a very different morphology. Around SMM3, [CII] becomes most prominent at the western edge of the mapped region, whereas for SMM4 it peaks to the north and SE of the PACS map. For both sources, the [CII] emission appears not associated with the outflow patterns traced by the molecular lines and the [OI] line at 63.2 μm. It may only be associated with the extended [OI] line pattern at 145.5 μm, to the west and SE edges of the maps around SMM3 and SMM4. [CII] is a common tracer of photon-dominated regions (PDRs, e.g. Dedes et al. 2010) and as such, it responds to a source of
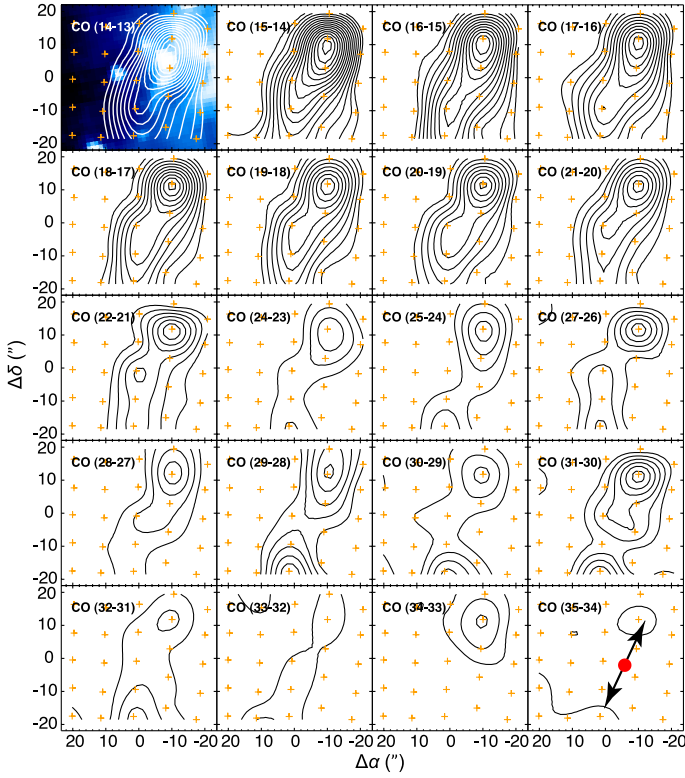
Fig. 6. Spectral line maps of the $J = 14 - 13$ up to $J = 35 - 34$ CO transitions around SMM3. All CO line maps presented show emission extending to the NNW and SSE from the exciting source near the center of each panel, with a strong peak towards the NW. The CO $J = 23 - 22$ transition is blended with the stronger $H_2O(4_{14}-3_{03})$ line and is therefore presented in Fig 8. The enhancement in the $J = 31 - 30$ map is due to blending with the OH $(3/2-3/2, 7/2^+-5/2^-)$ line. A $4.5\mu m$ Spitzer/IRAC image is presented as background on the upper left panel; bright regions correspond to H_2 emission which is spatially coincident with the CO peak. The filled circle and arrows in the lower-right panel display the position of the source (Harvey et al. 2007) and the direction of the outflows (Dionatos et al. 2010b). Contour levels are from 10^{-14} erg cm^{-2} s^{-1} and increase at steps of 10^{-14} erg cm^{-2} s^{-1} ($\sim$3-sigma of the weakest transitions)

UV radiation. Indeed, the emission west of SMM3 and north of SMM4 is consistent with a common UV source in the NW quadrant between the two PACS footprints (see Fig. 1). A possible candidate is SMM6, a binary, flat-spectrum source (Haisch et al. 2002; Winston et al. 2007) associated with energetic emission in Brγ and X-rays (Winston et al. 2007; Preibisch 2003). The bolometric luminosity of SMM6 ($\sim$13 L$_\odot$) is more than 10 times higher than SMM3 and SMM4 (Dionatos et al. 2010a). The PDR excitation of [CII] is further supported by the corresponding map recorded with ISO/LWS (upper right panel in their Fig. 3 of Larsson et al. 2002), which covers a larger area than the PACS observations in this paper: the kidney-shaped emission-maxima in [CII] for those maps extending from SMM6 to the SE towards SMM3 and SMM4 is consistent with the former being the exciting source. The [CII] emission mapped to the south of SMM4, is likely to be associated with a cluster of more evolved protostellar sources at the south (Winston et al. 2007; Harvey et al. 2007). In addition, the observed continuum morphology in Sect. 3.1.1, is consistent with the hypothesis of PDR excited [CII] emission, as the material becomes denser and more effectively shielded
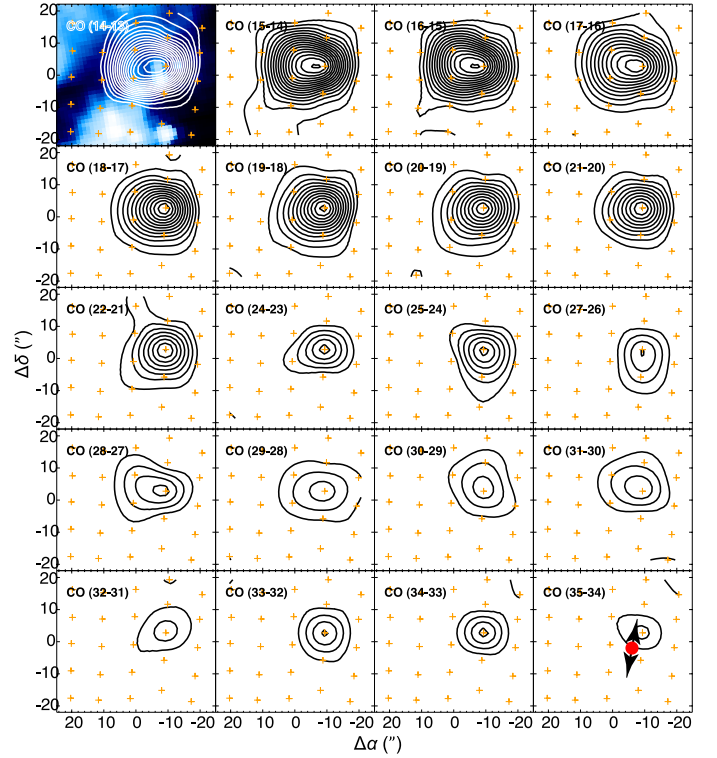

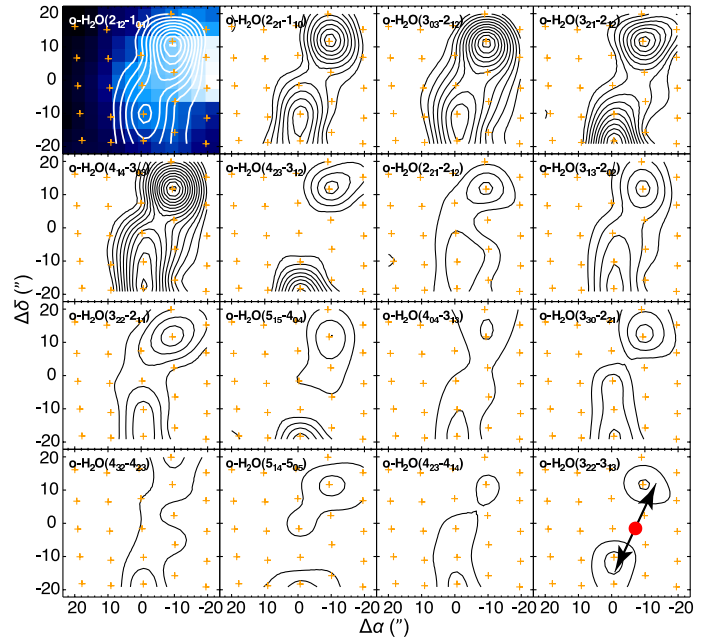**Fig. 7.** As in Fig. 6 for SMM4.

Fig. 8. Spectral line maps of the strongest water transitions detected by PACS towards SMM3. H_2O emission has very similar morphological characteristics to the CO maps (see Fig. 6), with the only exception traced to the SSE outflow from SMM3, where a secondary peak may be traced. Contour levels are as in Fig. 6.

towards the protostellar sources. The apparent resemblance between the morphology of the [CII] maps and the $70\mu m$ Spitzer image (right panel of Fig. 12) can be attributed to light recorded in the wide-band Spitzer filter originating from the same exciting source heating the ambient dust.

Table 1. *Herschel* - PACS line fluxes measured at selected positions of peak emission. Point-spread-function (PSF) corrections have been applied to the reported levels and errors are at 3-sigma level

Element	Transition	Wavelength (μm)	Flux (10^{-14} erg cm^{-2} s^{-1})			
			SMM3 b	SMM3 c	SMM3 r	SMM4 b
[OI]	$^3P_1-^3P_2$	63.1837	58.85±4.34	29.04±3.48	22.04±3.14	52.31±3.52
o-H$_2$O	$3_{30}-2_{21}$	66.4372	4.25±1.35	3.15±1.28	3.11±1.37	1.90±1.54
o-H$_2$O	$3_{30}-3_{03}$	67.2689	6.17±2.42	. . .	8.25±1.74	4.25±1.74
CO	$38-37$	69.0744	. . .	. . .	. . .	2.50±1.58
CO	$37-36$	70.9072	2.45±1.31	. . .	. . .	1.78±1.07
OH[a]	$^2\Pi_{\frac{1}{2}}-^2\Pi_{\frac{1}{2}}, \frac{7}{2}^- - \frac{5}{2}^+$	71.1708	2.62±0.24	. . .	. . .	3.05±0.45
OH[a]	$^2\Pi_{\frac{1}{2}}-^2\Pi_{\frac{1}{2}}, \frac{7}{2}^+ - \frac{5}{2}^-$	71.2158				
o-H$_2$O	$7_{07}-6_{16}$	71.9460	. . .	. . .	1.75±0.84	2.19±1.52
CO	$36-35$	72.8429	4.35±1.08	. . .	. . .	2.95±1.40
CO	$35-34$	74.8901	2.57±1.62	. . .	. . .	3.38±1.72
o-H$_2$O	$3_{21}-2_{12}$	75.3804	14.07±2.04	1.92±0.71	7.74±1.61	5.79±2.01
CO	$34-33$	77.0587	4.52±2.82	. . .	. . .	3.29±1.57
o-H$_2$O	$4_{23}-3_{12}$	78.7414	8.94±1.74	. . .	3.74±0.40	3.05±1.75
OH[a]	$^2\Pi_{\frac{1}{2}}-^2\Pi_{\frac{3}{2}}, \frac{1}{2}^- - \frac{3}{2}^+$	79.1173	6.35±1.91	2.10±0.70	. . .	4.44±0.54
OH[a]	$^2\Pi_{\frac{1}{2}}-^2\Pi_{\frac{3}{2}}, \frac{1}{2}^+ - \frac{3}{2}^-$	79.1809				
CO	$33-32$	79.3598	2.28±1.92	1.62±1.40	2.37±1.42	2.58±1.44
CO	$32-31$	81.8058	3.31±2.78	2.34±1.27	2.99±1.90	3.72±1.72
o-H$_2$O	$6_{16}-5_{05}$	82.0304	5.17±1.31	. . .	4.04±0.75	5.09±1.51
CO[a]	$31-30$	84.4107	9.55±1.75	4.13±0.63	1.73±1.44	5.53±1.65
OH[a]	$^2\Pi_{\frac{3}{2}}-^2\Pi_{\frac{3}{2}}, \frac{7}{2}^+ - \frac{5}{2}^-$	84.4199				
OH	$^2\Pi_{\frac{3}{2}}-^2\Pi_{\frac{3}{2}}, \frac{7}{2}^- - \frac{5}{2}^+$	84.5963	4.30±0.76	2.55±0.34	2.26±0.72	2.36±0.72
CO	$30-29$	87.1904	4.86±0.43	2.50±0.72	5.17±2.75	5.23±0.76
p-H$_2$O	$3_{22}-2_{11}$	89.9878	7.36±0.81	2.53±1.14	1.60±0.66	1.82±0.34
CO	$29-28$	90.1630	7.59±1.60	2.31±1.40	5.23±0.76	3.10±0.30
CO	$28-27$	93.3491	6.92±2.27	3.08±1.67	2.22±0.86	6.38±1.16
CO	$27-26$	96.7725	8.50±1.05	3.48±0.72	3.52±0.80	5.94±1.50
CO	$25-24$	104.445	7.01±0.98	2.48±1.15	2.19±1.10	9.63±1.18
o-H$_2$O	$2_{21}-1_{10}$	108.073	13.84±2.18	5.24±1.13	10.93±1.48	9.15±2.31
CO	$24-23$	108.763	7.96±1.78	2.66±0.39	1.81±0.33	8.25±1.18
CO[a]	$23-22$	113.458	24.84±1.07	13.60±1.12	15.73±0.68	22.95±0.56
o-H$_2$O[a]	$4_{14}-3_{03}$	113.537				
CO	$22-21$	118.581	11.01±0.79	6.60±0.31	5.30±0.34	12.79±1.31
OH	$^2\Pi_{\frac{3}{2}}-^2\Pi_{\frac{3}{2}}, \frac{5}{2}^- - \frac{3}{2}^+$	119.232	2.75±0.72	6.91±0.38	2.45±0.37	5.96±0.48
OH	$^2\Pi_{\frac{3}{2}}-^2\Pi_{\frac{3}{2}}, \frac{5}{2}^+ - \frac{3}{2}^-$	119.440	3.75±0.40	. . .	. . .	6.56±0.50
o-H$_2$O	$4_{32}-4_{23}$	121.719	1.30±.29	. . .	1.29±0.48	. . .
CO	$21-20$	124.193	14.06±0.49	8.44±0.55	7.22±0.42	16.44±0.37
p-H$_2$O	$4_{04}-3_{13}$	125.353	3.75±0.45	2.29±0.31	3.57±0.55	3.06±0.54
CO	$20-19$	130.369	15.83±0.35	9.01±0.40	8.88±0.35	18.49±0.30
o-H$_2$O	$4_{23}-4_{14}$	132.407	1.27±0.25	1.74±0.35	1.61±0.50	. . .
OH[a]	$^2\Pi_{\frac{1}{2}}-^2\Pi_{\frac{3}{2}}, \frac{7}{2}^- - \frac{9}{2}^+$	134.845	2.37±0.65	. . .	. . .	2.48±1.15
o-H$_2$O[a]	$5_{14}-5_{05}$	134.935				
OH[a]	$^2\Pi_{\frac{1}{2}}-^2\Pi_{\frac{3}{2}}, \frac{7}{2}^+ - \frac{9}{2}^-$	134.964				
CO	$19-18$	137.196	17.13±0.49	10.70±0.34	10.37±0.31	21.48±0.39
p-H$_2$O	$3_{13}-2_{02}$	138.527	8.48±0.43	5.41±0.49	7.66±0.29	7.43±0.33
CO	$18-17$	144.784	21.14±0.62	11.64±0.48	12.35±0.40	23.85±0.88
[OI]	$^3P_0-^3P_1$	145.525	4.09±0.53	2.83±0.44	3.22±0.25	4.74±3.37
CO	$17-16$	153.267	22.19±0.73	10.03±0.69	13.38±0.40	22.05±0.63
p-H$_2$O	$3_{22}-3_{13}$	156.193	. . .	. . .	2.17±0.90	2.29±0.80
[CII]	$^2P_{3/2}-^2P_{1/2}$	157.741	3.45±0.52	1.01±0.49	4.52±1.54	3.29±0.37
CO	$16-15$	162.812	26.34±0.63	12.12±0.73	16.97±1.06	29.81±0.59
CO	$15-14$	173.631	32.60±1.19	18.10±0.58	17.78±0.76	33.71±0.93
o-H$_2$O	$3_{03}-2_{12}$	174.626	16.76±1.08	6.89±0.69	9.52±0.73	16.45±0.63
o-H$_2$O	$2_{12}-1_{01}$	179.527	26.61±0.59	11.15±0.79	16.81±0.90	23.93±0.65
o-H$_2$O	$2_{21}-2_{12}$	180.488	7.54±0.68	4.65±1.40	6.02±0.54	5.09±0.59
CO	$14-13$	185.999	30.53±0.90	17.04±0.41	19.11±0.74	37.83±0.62

blended lines

3.1.4. Line emission pattern

The morphology of the line emission presented in the maps of the previous section shows different characteristics for SMM3
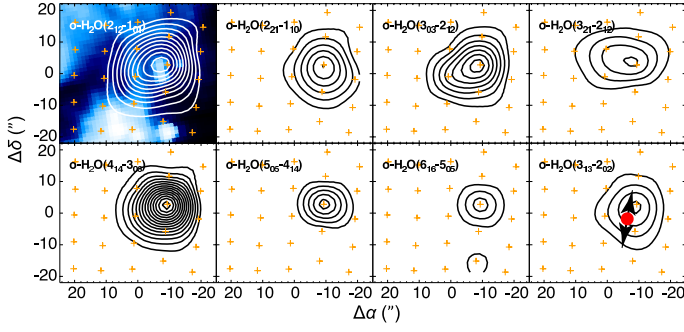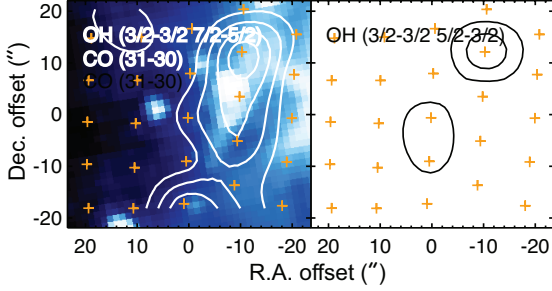
Fig. 9. As in Fig. 8 for SMM4.

Fig. 10. Extended OH emission around SMM3. Contour levels are as in Fig. 6.
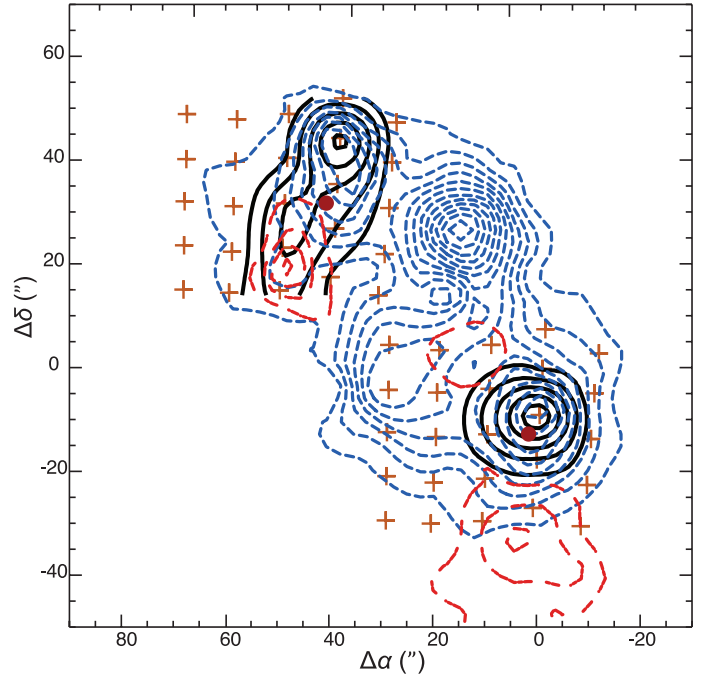

Fig. 11. CO $J = 18 - 17$ emission observed with Herschel/PACS (black continuous contours) superimposed on high velocity CO $J = 3 - 2$ blue-shifted (blue, short-dashed contours) and red-shifted (red, long-dashed contours) emission from JCMT/HARP-B (Dionatos et al. 2010b). Positions of the PACS spaxels are indicated with (orange) crosses, and the locations of SMM3 and SMM4 with (red) filled circles. Peaks of low and high J CO emission are coincident.

and SMM4. To quantify whether the emission is point-like or extended compared to the nominal PACS spaxel size (9.4″), we employ the POMAC code (Lindberg & the DIGIT team 2013, see also Appendix B), which performs a deconvolution of the observed emission pattern with the instrumental point-spread function (PSF). The code is based on a modified version of the CLEAN algorithm (Högbom 1974) with the difference that it requires the positions of testing "point" sources. Such points in the present case are selected to be the spaxels displaying emission maxima. The code was run iteratively on the resulting residual maps of the previous clean process in the same fashion, until reaching residual maps showing no significant emission. The results from this analysis are presented in Fig. 13 for the CO (18-17) line maps around SMM3 and SMM4.

The results of the cleaning process suggest that most of the line emission around SMM3 is confined within 3 spaxels, towards the NW (blue peak), the center and to the S (red peak), which are named hereafter SMM3b, SMM3c and SMM3r. Excluding any of these points from the cleaning process results in significant residuals at the location omitted, indicating that the emission arises from unresolved regions within each spaxel. In the case of SMM4 most the observed emission originates from a single spaxel coinciding with the blue-shifted lobe and named SMM4b (see also Fig. 13). Line fluxes for the molecular and atomic species observed with PACS are reported for these points in Table 1. The following sections focus on the analysis of individual spaxels indicated from the clean process.

3.2. Spitzer

Spitzer/IRS maps encompass the whole SE region of the Serpens Cloud Core, at resolutions ranging between 3.5″ to 10.5″ for the SL and LL modules, respectively (see also Sect. 2). A line intensity map at 3.5″ resolution of the 0-0 S(5) pure rotational transition of molecular hydrogen is presented in Figure 14.

Superimposed on this, yellow and white contours corresponding to high velocity CO $J = 3 - 2$ blue- and red-shifted outflow gas from (Dionatos et al. 2010b) show a clear spatial association between H_2 and entrained gas traced by low-J CO. In the same figure, the positions of protostellar sources extracted from the catalogue of Winston et al. (2007) are also indicated. The close association between low-J CO and H_2 emission is also seen in the outflows of L1157 (Nisini et al. 2010). Serpens maps with ISO/CVF (Larsson et al. 2002) at 7 μm show substantial emission around the SW clump, with significant enhancements to the north of SMM3 and close to SMM6, which are in good correspondence with the morphology shown in Fig. 14. The full Spitzer emission line maps for all the detected H_2 and forbidden atomic transitions from [FeII], [SiII] and [SI] are presented in Appendix A.
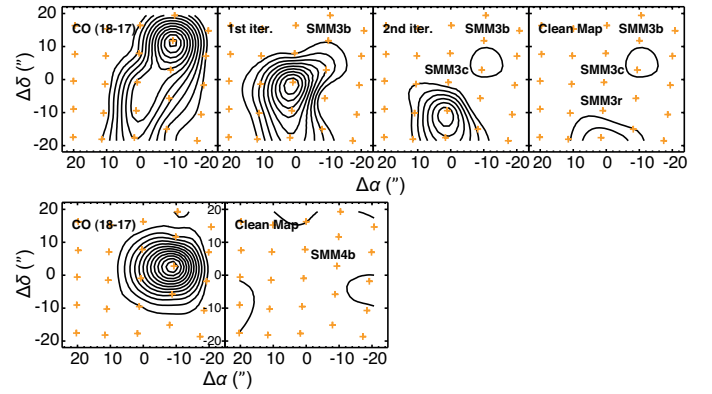
3.2.1. H_2 emission

Maps of the H_2 rotational ladder from the S(0) to the S(7) rotational transitions around SMM3 are shown in the upper panel of Fig. 15 after resampling to match the PACS resolution. The S(0) and S(1) transitions display emission in a diffuse, elongated structure, roughly resembling the outflow pattern traced with CO and H_2O and [OI]. Similar diffuse H_2 emission has been observed in protostellar environments for a number of other Spitzer spectral scan studies (e.g. Maret et al. 2009; Dionatos et al. 2010a). In SMM3, higher energy transitions between S(2) and S(7) show an outflow distribution similar to that observed in CO, with a secondary peak at the southern lobe as seen in H_2O.

Table 2. *Spitzer* - IRS line fluxes measured at selected positions of peak emission. Reported errors are at 3-sigma level.

Element	Transition	Wavelength (μm)	Flux (10^{-14} erg cm^{-2} s^{-1})			
			SMM3 b	SMM3 c	SMM3 r	SMM4 b
H_2	$0-0$ S(7)	5.5111	23.17±0.83	2.94±1.25	5.46±1.03	17.35±0.77
H_2	$0-0$ S(6)	6.1085	11.59±1.04	2.29±1.45	5.34±1.45	9.82±0.62
H_2	$0-0$ S(5)	6.9095	48.55±1.24	5.94±1.83	9.86±1.90	26.30±1.07
H_2	$0-0$ S(4)	8.0251	16.40±4.34	2.05±1.10	5.42±1.24	17.40±2.13
H_2	$0-0$ S(3)	9.6649	20.47±0.43	5.74±0.27	6.78±0.28	7.57±0.47
H_2	$0-0$ S(2)	12.278	6.58±0.42	1.36±0.31	3.44±0.49	7.75±0.37
H_2	$0-0$ S(1)	17.039	5.68±0.40	5.22±0.59	4.51±0.14	2.31±0.25
[SI]	$^3P_1-^3P_2$	25.249	3.90±0.52	4.21±0.30	3.51±0.24	3.51±0.34
[FeII]	$^6D_{7/2}-^6D_{9/2}$	25.988	2.20±0.25	0.68±0.18	. . .	1.83±0.08
H_2	$0-0$ S(0)	28.218	3.77±0.16	2.09±0.21	2.90±0.17	1.52±0.06
[SiII]	$^2P_{3/2}-^2P_{1/2}$	34.815	5.17±0.61	2.56±0.21	3.19±0.22	6.24±1.37
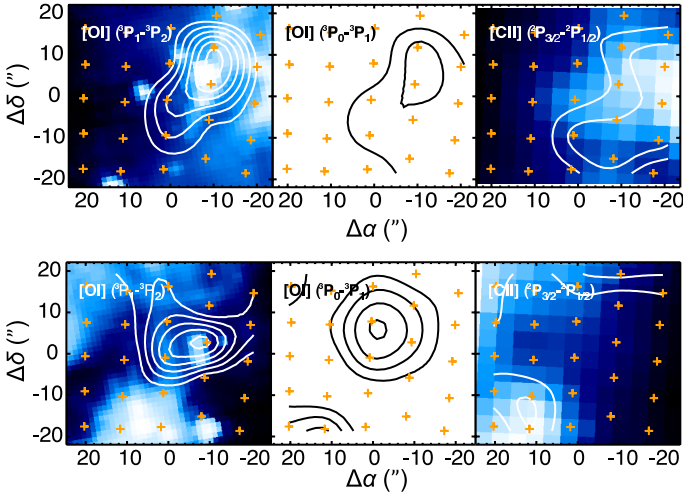
Fig. 12. Spectral line maps for the atomic lines detected with PACS around SMM3 and SMM4 (upper and lower panels, respectively). Oxygen lines follow the outflow pattern shown in molecular line maps while [CII] cannot correlate with the outflow morphology. Contour levels are as in Fig. 6 except for the [OI] $^3P_1$ - $^3P_2$ maps which are from 10^{-14} erg cm^{-2} s^{-1} with increments of 5×10^{-14} erg cm^{-2} s-1. Background images are 4.5 μm from Spitzer/IRAC (left panels) and 70 μm Spitzer/MIPS (right panels), display associations with the corresponding superimposed atomic lines.

Fig. 13. Deconvolution of the CO (18-17) maps around SMM3 and SMM4 with the instrumental point-spread function. The leftmost panel presents the initial line map, and stepwise to the right each presents the residual map after subtracting the instrumental PSF at a specific location. For SMM3 (upper panels), such locations are indicated on each panel (SMM3b, SMM3c and SMM3r). In SMM4 (lower panel) the emission is confined to a single spaxel (SMM4b). The rightmost panel corresponds to the final residual map where flux levels are at ~ 10% or lower compared to the peak values in the original maps.

3.2.2. Atomic emission

Figure 16 presents line maps from the fundamental transitions of [FeII], [SiII] and [SI] detected with Spitzer around SMM3 (top panel) and SMM4 (lower panel). [FeII] and [SiII] lines peak at NW of SMM3, at the same region as most of the molecular and atomic lines. In contrast, the [SI] map around SMM3 delineates the outflow morphology showing clearly both the blue and the red-shifted lobes. In the case of SMM4, all atomic lines peak far from the source position, showing a similar morphology as the molecular species traced by PACS. Atomic line fluxes are reported in Table 2.

4. Analysis

4.1. Excitation conditions

The physical conditions of the excited gas may be directly constrained by means of excitation diagrams, i.e., plots of the logarithm of the column density over the statistical weight as a function of the upper level energy for a range of transitions of

Similarly, the resampled IRS map at the PACS scale around SMM4 is shown in the lower panel of Fig. 15. As in the case of SMM3, the S(0) and S(1) H_2 transitions show diffuse, unconfined emission. The higher energy transitions (S(2)-S(7)) present a strong peak located at the same position as in the PACS molecular line maps and an elongated structure towards the N, having no clear association with the outflow structure mapped with any other tracer (e.g. low-J CO, interferometric maps). This is similar to the structure observed in the $^3P_1$-$^3P_2$ [OI] transition map (63 μm) and may be interpreted as gas excited by some of the surrounding protostellar sources. Besides this exception, the H_2 emission around SMM3 and SMM4 shows a pattern that is very similar to those of CO, H_2O and [OI]. H_2 line fluxes for the same positions as in Table 1 are listed in Table 2.
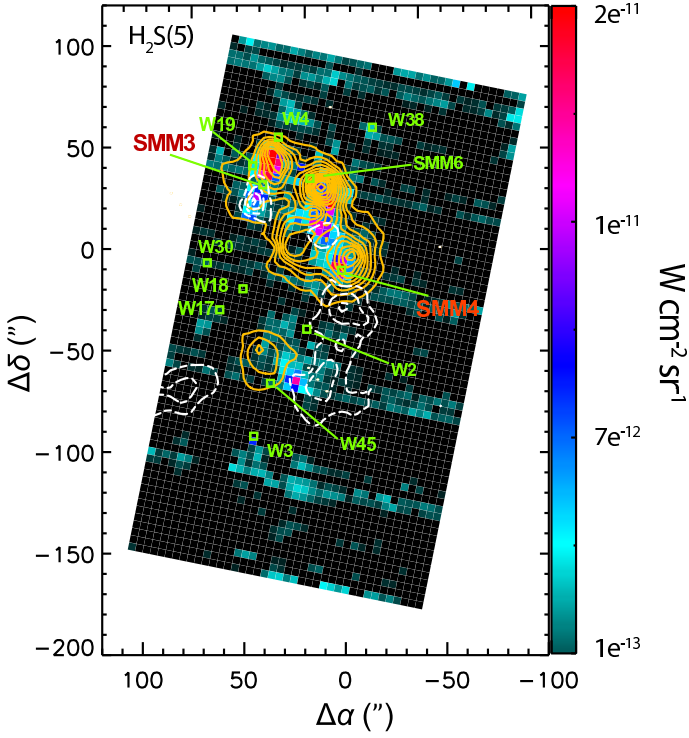
Fig. 14. Spitzer spectral map of the Serpens SE region in H_2 0-0 S(5) line emission; color coded flux levels are indicated on the side bar. Dim stripes in the horizontal direction are residuals due to rogue pixel contamination of the IRS detectors. Yellow and white contours delineate high velocity blue- and red-shifted $J = 3 - 2$ CO gas from Dionatos et al. (2010b), showing a strong spatial correlation in the excitation between the two species. Positions of known protostellar sources from the catalogue of Winston et al. (2007) are indicated on the map.

one species. Assuming that the transitions are optically thin, the populations of the upper states can be calculated simply from the line fluxes and their logarithms can be plotted versus the upper state energy. If a straight line can be fitted to these points, a rotational temperature (T_{rot}) can be found from the slope (e.g. Goldsmith & Langer 1999). T_{rot} represents the common excitation temperature of the levels considered and need not be the same as the kinetic temperature (T_K) (e.g., Neufeld 2012), but is the correct temperature to use in the partition function. Together with the intercept, the partition function can be used to get the column density or total number of molecules in all levels. One can also estimate the ortho-to-para ratio of molecules such as H_2 and H_2O for which a number of lines are observed in the same wavelength range for both the ortho and para spin-states.

For the applications discussed in the following, upper level energies and Einstein coefficients were adopted from the JPL[2] and CDMS[3] catalogs (Pickett et al. 1998; Müller et al. 2005, respectively). Partition functions for different temperatures were retrieved from the same databases interpolating for the corresponding T_{rot} with the exception of hydrogen where it was calculated by summing up the first 35 energy levels of the molecule.

We employ excitation diagram diagnostics for the CO, H_2O and OH lines detected with Herschel/PACS, as well as H_2 detected with Spitzer/IRS to constrain the physical conditions for each molecule. Column densities were estimated from the

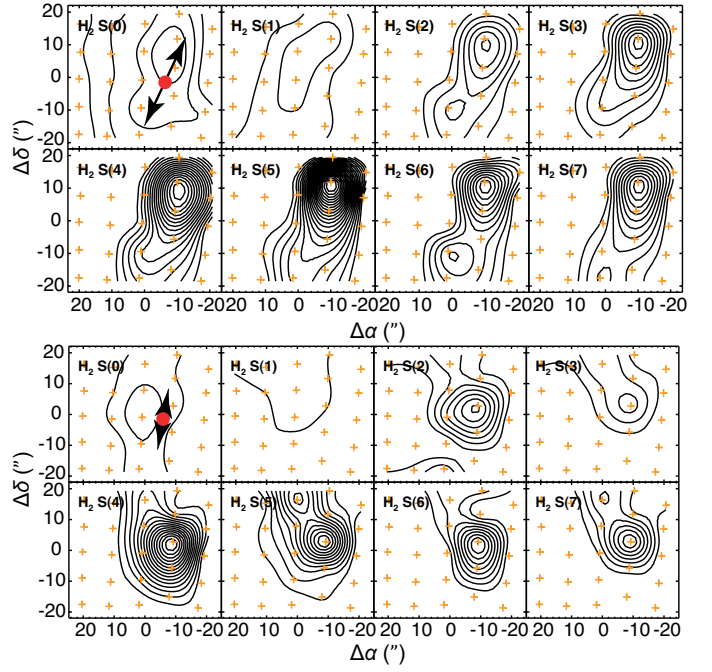**Fig. 15.** Spitzer spectral maps of the H_2 rotational transitions around SMM3 (upper panels) and SMM4 (lower panels), resampled on the PACS footprint pattern. The 0-0 S(0) and S(1) transitions show diffuse emission. Higher energy transitions display the outflow pattern as in the case of CO and H_2O, except for SMM4, where the extension to the north is only traced in [OI] (see Fig. 12). Contours start at 10^{-14} erg cm^{-2} s^{-1} and increase at 10^{-14} erg cm^{-2} s^{-1} steps.
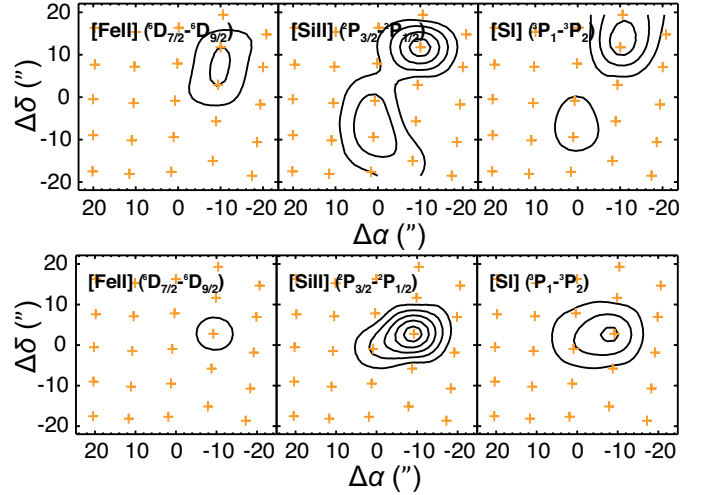

Fig. 16. As in Fig. 15, for the atomic lines detected by IRS.

PACS line fluxes reported in Tables 1 and 2 focusing on the regions where the molecular emission is most prominent (see Sect. 3.1.4). Fig. 17 shows the excitation diagrams for the blue shifted lobe at NW of SMM3 (SMM3b); diagrams corresponding to other positions discussed here are presented in Appendix C.
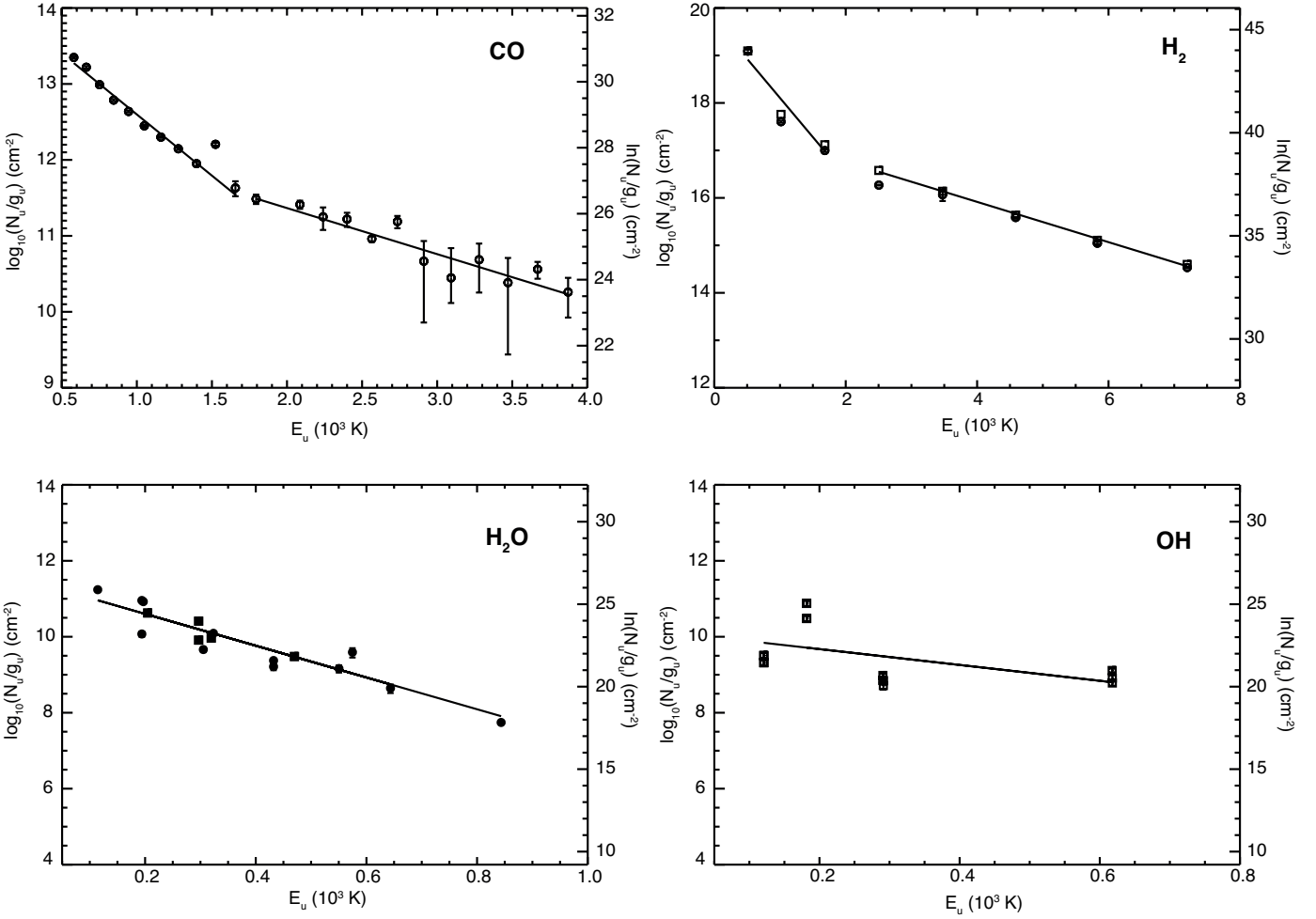
Fig. 17. Excitation diagrams for the molecular emission towards SMM3b. Column densities are given in base 10 and natural logarithms in the left and right hand sides of each plot. CO (top left) and H_2 (top right) plots show a break at E_u ~1600 K defining a "warm" and a "hot" gas component at temperatures ~300K and 900K, respectively. H_2O (lower left) and OH (lower right) display lower temperatures at ~100 K and high scatter of data points, which indicates that some transitions are optically thick and/or subthermally populated.

In the CO excitation diagram (upper left panel of Fig. 17) the distribution of observed data points displays a break for upper level energies of E_u ~1700 K. This break suggests the existence of two distinct regions which correspond to different physical conditions. These regions are fit separately with straight lines, excluding any blended CO lines as listed in Table 1. The two components correspond to temperatures of ~270 K and ~715 K, and column densities of 1.6×10^{16} and $9.8 \times 10^{14} cm^{-2}$, assuming that the emission fills the spaxel. The same two-component trend is found for all the other positions examined, with the break point always located at E_u ~1700 K. Derived temperature and column density values for the on-source and outflow positions are reported in Table 3, displaying in all cases both a warm ($T \sim 250$ K) and a hot ($T \sim 800$K) components, with an average of 25 times higher column density in the warm component.

Fitting the CO data with two linear segments separated at E_u ~1700 K is a commonly used method (e.g. Herczeg et al. 2012; Green et al. 2013) under the assumption that the emission is optically thin. Neufeld (2012) has demonstrated that at sufficiently high temperatures and for densities below the critical, the excitation pattern of CO at a single kinetic temperature shows a broken power-law pattern that can reproduce the observed distribution. This possibility has been examined for SMM1 in Serpens

and B335 that display a similar excitation pattern to the Serpens sources of this work (Goicoechea et al. 2012; Green et al. 2013, respectively). In both cases they find that solutions can be obtained for $n(H_2) = 10^4$ cm^{-3} and $T \sim 3000$K. While low densities are predicted by shock models (Sect. 4.2), high temperatures are possible if CO does not trace the same gas as H_2 (see discussion below). Neufeld (2012) also examines the possibility that a positive curvature can be also obtained for an admixture of gas at different temperatures. Such conditions are commonly found to occur in shocks (see Sect. 4.2) and are also consistent with the H_2 ortho-to-para ratios lying below the equilibrium value of 3, as discussed below. From the CO excitation diagrams alone it is not possible to distinguish between these solutions.

Table 3. CO rotational temperatures and column densities

Position	T_1 (K)	T_2 (K)	N_1 (10^{16} cm^{-2})	N_2 (10^{14} cm^{-2})
SMM3b	270±10	715±75	1.6±0.2	9.8±1.4
SMM3c	260±10	750±80	0.9±0.15	3.8±0.9
SMM3r	230±10	1020±280	1.4±0.14	2.3±2.5
SMM4	270±10	720±50	1.8±0.2	9.4±2.0

11

In the case of molecular hydrogen, an estimate of the visual extinction and the ortho-to-para ratio can be derived following the method described in Wilgenbus et al. (2000). The statistical weight g_u for H_2 includes the spin degeneracy term ($2S + 1$, with $S = 0$ for para and $S = 1$ for ortho states). Differences from the LTE value in the ortho-to-para ratio will then be reflected as vertical displacements between the ortho and para transitions in the excitation diagram, forming a "saw-tooth" pattern. The observed ortho-to-para ratio is estimated from the displacement of the S(5) line, in comparison to the levels of S(4) and S(6). For the extinction, the calculation is based on the fact that the S(3) pure rotational level at 9.7μm is particularly sensitive to the interstellar extinction, as it is located within the wide-band silicate absorption feature centered at the same wavelength; therefore column density displacements of this line compared to other hydrogen transitions can provide information on the extinction, which can be related to visual extinction assuming an $A_{9.7}/A_V$ ratio equal to 0.087 (Rieke & Lebofsky 1985).

The upper right hand panel of Fig. 17 shows the H_2 excitation diagram at SMM3b, in which observed line fluxes were corrected for an interstellar extinction of A_V=8.2 mag (open squares), derived from the displacement of the S(3) pure rotational level. In addition, the H_2 S(0) and S(1) line intensities were corrected for diffuse emission, after estimating an average value from the positions not associated with known outflows (see Fig. A.2). As in the case of CO, a similar break is seen at E_{up} ~1500 K, which separates data points into two temperature components, corresponding to ~260 K and ~1000 K with estimated column densities of 6.3×10^{20} and 1.1×10^{19} cm^{-2}, respectively. Excitation diagrams for other positions of interest are presented in Appendix B, and derived values for the corresponding physical conditions are listed in Table 4. In all cases, molecular hydrogen traces gas separated into a "warm" and a "hot" component, each one tracing, within uncertainties, similar column densities between different positions. In contrast, SMM4 has an A_V twice as high and ortho-to-para ratio about half of the equilibrium value of 3 compared to SMM3 (see also Fig. C.2). The ortho-to-para ratio is here estimated for lines tracing the "hot" component, and may not be representative for the "warm" gas.

The positive curvature observed in the CO excitation diagram may be attributed in effects other than a distribution of temperatures. As mentioned already, Neufeld (2012) has shown that for CO, an isothermal medium with low gas density can explain the observed distributions. However, Neufeld (2012) argues that a similar distribution in H_2 cannot be produced by an isothermal medium. In the next section we examine the relation of CO to H_2, and argue that both molecules trace the same gas corresponding to a distribution of temperatures rather than a very hot isothermal medium with low density.

In an analogous study of the outflow emerging from SMM1 in Serpens, Goicoechea et al. (2012) find a similar temperature structure, with an additional cold component traced by CO lines with $J_{up} \leq 14$ (observed with SPIRE). Reported column densities are about 2 orders of magnitude higher for both the "warm" and "hot" components in SMM1 than corresponding ones reported here. This difference can be interpreted in terms of the smaller emitting area of 4″ assumed and the estimating method, which is based on non-LTE analysis. The CO column density ratio of the "hot" and "warm" components in both studies is ~20 indicating that despite the different approaches, the relative contribution of the two components remains invariable. Analysis of Spitzer data around other embedded protostellar sources (e.g. NGC1333, HH211 and L1448, Maret et al. 2009; Dionatos et al.

Table 5. H_2O and OH rotational temperatures and column densities.

Position	T_{H_2O} (K)	T_{OH} (K)	N_{H_2O} (10^{12} cm^{-2})	N_{OH} (10^{12} cm^{-2})
SMM3b	105±20	200±80	9.7±2.2	1.1±1.8
SMM3c	120±25	⋯	4.1±2.8	⋯
SMM3r	105±20	⋯	7.6±4.1	⋯
SMM4b	88±10	160±60	8.2±3.9	1.4±2.3

2010b; Nisini et al. 2010, respectively) find a very similar excitation structure for molecular hydrogen, indicating that such excitation conditions are common around embedded protostars.

H_2O and OH excitation diagrams are presented in the two lower panels of figure 17. Both molecules show significant scatter over column densities. For water this effect may indicate that a number of lines are optically thick or subthermally populated (e.g. Herczeg et al. 2012). In the case of OH, subthermal excitation and IR pumping have been found to be responsible for the observed scatter (Wampfler & the WISH team 2012). Emission from water vapor around SMM3 and SMM4 is associated with gas at temperatures ~100 K and column densities of ~ $5 - 10 \times 10^{12}$ cm^{-2}. Corresponding temperatures for OH are 50-100% higher and column densities are about an order of magnitude lower (see Table 6). However, the large scatter in the diagram unavoidably leads to higher uncertainties, and the values given here should only be considered as rough estimates.

4.1.1. Relation between CO and H_2

CO is the most common tracer of protostellar outflows. It is easily excited even at low temperatures found in quiescent molecular clouds (T ~20 K) and its lower energy transitions ($J_{up} < 7$) are readily accessible from ground-based observatories. Due to these properties, CO is commonly used as a proxy for the more abundant H_2, which, as a light homonuclear molecule, is only excited in energetic environments. The determination of the total amount of H_2 from measurements of CO is commonly assessed under the assumption that the CO/H_2 abundance ratio is almost constant and equal to 10^{-4}, as measured by Watson et al. (1985).

The majority of available direct measurements of the CO/H_2 ratio rely on observations of far-ultraviolet absorption lines from both molecules superimposed on the spectra of background stars in diffuse clouds (e.g. van Dishoeck & Black 1987). For dense clouds, attempts to measure the CO/H_2 ratio focus on the simultaneous study of the near-infrared (NIR) CO and H_2 rovibrational lines in absorption (e.g., Lacy et al. 1994) so it is not obvious that these tracers sample the same volume of gas (for a review of the topic see also van Dishoeck et al. 1992).

The analysis of the CO and H_2 excitation conditions (§4.1 above) indicates that their emission originates in gas with very similar characteristics; both molecules trace a two-temperature structure with a "warm" and a "hot" component at T_{warm}~ 300 K and T_{hot}~1000 K, respectively. At the angular resolution of the observations (9.4″, PACS) the emission pattern of both molecules is tightly correlated (Fig. 18). This set of common characteristics suggests that the CO and H_2 emission originates from the same physical processes occurring within the same volume of gas. Therefore the ratio of the column densities calculated from the excitation analysis corresponds to the abundance ratio of the two molecules. Still, even the warm component examined here lies at much higher temperatures than the quiescent gas in molecular clouds ($T \sim 20$ K) and therefore the ratios estimated here apply only in highly excited gas.

Table 4. Physical conditions derived from the H_2 excitation diagrams

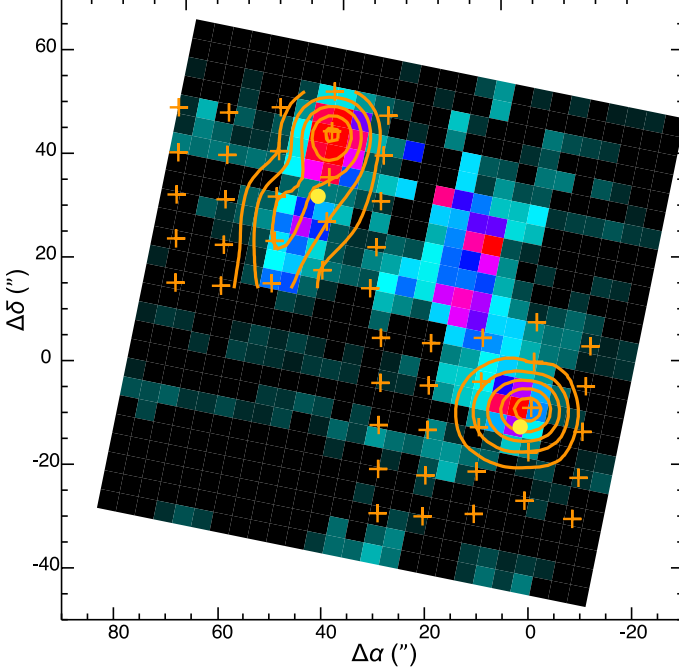| Position	T_1 (K)	T_2 (K)	N_1 $(10^{20} cm^{-2})$	N_2 $(10^{18} cm^{-2})$	A_V (mag)	OPR
SMM3b	260±8	1025±25	8.1±0.6	11.0±0.7	8.8	3.0
SMM3c	210±5	970±50	7.5±0.2	1.5±0.5	2.0	2.8
SMM3r	250±5	970±90	8.0±1.3	4.7±1.7	10.5	1.7
SMM4b	355±15	1000±80	9.5±0.4	14.0±4.7	20.0	1.7

Fig. 18. CO $J = 18 - 17$ emission (orange contours) superimposed on the H_2 S(5) line map around SMM3 and SMM4, displaying the strong spatial correlation between the two molecular tracers. The positions of SMM3 and SMM4 are marked with filled yellow circles. Color encoding for the hydrogen map is as in Fig. 14 and levels for the carbon monoxide as in Fig. 6 and 7.

Table 6. CO/H_2 column density ratio

Position	$(N_{CO}/N_{H_2})_{warm}$ (10^{-5})	$(N_{CO}/N_{H_2})_{hot}$ (10^{-5})
SMM3b	2.0±0.16	8.9±1.4
SMM3c	1.3±0.16	24.9±10.3
SMM3r	1.8±0.19	4.9±3.6
SMM4b	1.9±0.15	6.7±2.7

Estimates of the CO/H_2 ratio are given in Table 6. Values around ~1.8×10^{-5} for the "warm" gas and from ~5×10^{-5} up to ~2.5×10^{-4} for the "hot" gas show a significant discrepancy of the ratio between the two physical components. Despite the rather high uncertainties, these estimates are indicative of a higher abundance ratio by a factor of 3 – 10 in the "hot" gas compared to the "warm" component.

Our estimations rely on the assumptions that the lines are optically thin and that the two molecules trace the same volume of gas. The similarity of the temperatures of the two components for CO and H_2 support the second assumption. Further, since the H_2 levels are likely in LTE, and the T_{rot} of the CO levels are similar for warm and hot components, the CO is likely in LTE as well ($T_K = T_{rot}$), making the Neufeld solution unlikely. For the "warm" component, the main source of uncertainty in the CO/H_2 ratio is the accuracy in the derivation of the H_2 column

densities, while the "hot" component is more affected by low signal-to-nose ratio in the CO lines with $J_{up} > 31$.

As discussed in Sect. 4.1 the line fluxes from the S(0) and S(1) H_2 transitions have been corrected for diffuse emission. This "cold' ' emission is likely associated with the CO emission arising from $J_{up} < 14$, tracing larger-scale outflows. After being corrected, the S(0) point may still maintain some contribution from this colder component (see Figs. 17, C.1 C.2). Assuming that this contribution is still dominating the S(0) emission, we derive physical properties of the "warm" component using the S(1) - S(3) lines. In that case the H_2 temperature is ~ 80% higher than reported in Table 4 ranging between 400 and 600K. the The corresponding H_2 column density is an order of magnitude lower, resulting in a CO/H_2 ratio ~ 2×10^{-4}, a factor of 2 higher than "nominal" value. For the derived conditions, H_2 corresponds to an intermediate component between "warm" and "hot", which renders invalid our assumption that CO and H_2 trace gas at very similar conditions. Therefore the ratio obtained by discarding the S(0) sets an upper limit to our estimations of CO/H_2.

The high levels of the S(0) line relative to the S(1) and S(2) can also be interpreted in terms of non-equilibrium values of the ortho-to-para ratio. The ratio depends strongly on temperature, and can be significantly smaller than the equilibrium value of 3 for colder gas (e.g. Neufeld et al. 2009). For non-equilibrium values of the ortho-to-para ratio will be reflected as a vertical displacement between the ortho and para transitions in the excitation diagram. In that case, it is the S(1) data point lying at lower levels with respect to the S(0), rather than the latter data point being affected by diffuse emission. The ortho-to-para ratio values estimated here are representative of the "hot" gas and may not apply for the "warm" component. If the "hot" gas has not reached the equilibrium ortho-to-para value, it would be even more so for the "warm" component. Indeed, for the positions that the "hot" ortho-to-para ratio is found below 3, the relative displacement between the S(0) and S(1) lines even more pronounced. (Figs. C.1, C.2). In this case the derived "warm" H_2 column densities would be underestimated and the CO/H_2 ratio in the "warm" gas would be lower.

In comparison with analogous studies our estimates are different compared to the ratio of ~ 2×10^{-4} found for ~50 K gas in Lacy et al. (1994), but fall within the limits of log(CO/H_2) between -7.58 and -4.68 measured by Sheffer et al. (2008).

4.2. Comparison with shock models

The outflow morphologies of the maps in Sect. 3 suggest that the bulk of the line emission is likely produced in shocks. Emission is traced down to ~10″ from the source, which corresponds to ~4000 A.U. for the adopted distance. Therefore some contribution from gas in the envelope which is heated-up by UV photons from the protostar cannot be excluded, albeit this is not suggested by the [C II] morphology. In order to further examine these arguments and to constrain the underlying physical conditions, we compare the observed line emission

Table 7. Parameters of the shock models employed

Model	KN'96	FPDF'10
v_s (range, km s^{-1})	$5 - 40$	$10 - 40^a$
v_s (step, km s^{-1})	5	10
n (range, cm^{-3})	$10^4 - 10^{6.5}$	$2 \times 10^4 - 2 \times 10^5$
n (step, cm^{-3})	$10^{0.5}$	10
J-shocks	no	yes
H$_2$ lines	full	full
CO lines	full	$J_{up} \leq 20$
H$_2$O lines	limited	full
[OI] lines	no	full

^{a} $10 - 30$ km s^{-1} for J-shocks

to the shock model predictions of Kaufman & Neufeld (1996) and Flower & Pineau des Forêts (2010) (hereafter KN'96 and FPDF'10, respectively). Both models provide line intensity predictions for H$_2$, CO, and H$_2$O for steady-state shocks. KN'96 models include a more extensive and refined grid of shock velocities and pre-shock densities but only for C-type shocks, while FPDF'10 models include predictions for J-type shocks, however for a coarser grid of input parameters. Major differences between the two codes is in the treatment of the chemistry and the collisional rate coefficients for the CO and H$_2$O. As reported in FPDF'10, their models include charged grains, which act to compress the shock front and increase the temperatures reached. The basic set of values for the grids of predictions provided by the two models are summarized in Table 7. For the purposes of the current study, the predictions provided by the codes can be treated as complementary.

Model grids are compared to line intensities through χ^2 fits to optimally reproduce the observed line emission for different molecules. Comparisons are performed considering relative line intensities, introducing a scaling factor (beam filling factor). This factor accounts for the possibility that the emitting region is smaller than the instrumental beam, which equals to the PACS spaxel size in this study. As a general trend, the C-shock models can reproduce the observed line intensities only if model predictions are scaled for a small beam-filling factor, while J-shock models require a scaling factor much closer to unity. The beam filling factor along with the uncertainties in the fluxes of the observed lines result in degenerate model solutions.

4.2.1. H$_2$ & CO

Comparisons between H$_2$ and CO intensities at SMM3b and best fitting models are presented in Fig. 19 (upper and middle panels). As a general trend we find that C-shock models cannot simultaneously reproduce the full range of observed lines. The only exception is the FPDF'10 CO model predictions, which are limited to $J_{up} = 20$ and therefore do not cover to the same extent the CO transitions observed. For C-shocks, the transitions corresponding to the two temperature components are therefore fitted independently. For each molecule and temperature component, best fitting models provide similar solutions for the density and shock velocity at each position of peak intensity, reflecting a consistent curvature and slope in the excitation diagram between the different regions. In contrast, the beam filling factor which scales the model intensities (as expressed in terms of column densities over degeneracy in the excitation diagrams) relative to the observed ones varies up to two orders of magnitude between different positions and temperature components (see Tab. 8).

C-shock models predictions from KN'96 and FPDF'10 provide solutions which are substantially different for the two molecules, or even the two temperature components of the same molecule. Degenerate model solutions complicate significantly the interpretation of the predicted values, however a few trends can be recognized. The two models provide consistent predictions on the shock velocity. This ranges from low ($10 - 15$ km s^{-1}) and moderate (20 km s^{-1}) values for the "'warm" and "hot" H$_2$ components, to high values ($30 - 40$ km s^{-1}) for all CO temperature components. For both models, beam filling factors vary up to an order of magnitude even for the same set of velocities and pre-shock densities in order to accommodate the observed values at different positions along the outflows. Furthermore, lower beam filling factor values correspond to higher densities and *vice versa* indicating degenerate solutions. In the case of CO, KN'96 models provide equally good (degenerate) solutions for a set of models with stepwise increasing density by 0.5 dex and decreasing velocity by 5 km s^{-1}.

Predictions for J-shock models from the grid of FPDF'10 are presented on the upper-right and middle panels of Fig. 19. Single-temperature J-shock models are able to reproduce the full range of H$_2$ transitions (with the exception of S(0)). The corresponding models imply low pre-shock densities of 2×10^4 cm^{-3} and a moderate shock velocity of 20 km s^{-1}, for all positions examined. For CO, predicted line intensities in the FPDF'10 grid are limited to $J_{up} = 20$ so no secure conclusions can be made on the shock type. However comparisons show that J-type shocks provide essentially the same set of solutions for both the CO and H$_2$ emission. Beam filling factors vary from 30% to 90%, with higher values corresponding to the points of peak emission. Such filling factors can be explained by a chain of unresolved shock knots within the PACS spaxel size.

The emission in the 4.5μm IRAC image presented in Fig. 12 (upper left panel) is dominated by higher excitation H$_2$ transitions (Neufeld et al. 2006) and therefore can give a rough measure of the size of the emitting regions. The bright emission structures around SMM3b and SMM4b appear to be close to 10-30% of the PACS spaxel size and therefore higher beam filling factors predicted by the FPDF'10 models are more plausible in describing better the physical conditions therein. For the positions of SMM3c and SMM3r, models predict lower beam filling in comparison to the regions of brightest emission which is consistent with the smaller/dimmer structures observed in the IRAC image. In conclusion, J-shock models with pre-shock densities of 2×10^4 cm^{-3} and velocities of 20 km s^{-1} can simultaneously reproduce both CO and H$_2$ emission. The predicted size of the emission region from these solutions is consistent with those indicated by imaging.

4.2.2. H$_2$O & OH

The lower panels of Fig. 19 presents the best fitting models from the KN'96 grid in comparison with the H$_2$O observations. Since the KN'96 model grid was intended for comparisons to ISO observations, the number of water lines available is limited to the brightest transitions. Values derived from the comparison suggest a C-type shock of low density and high velocity (10^4 cm^{-3}, $30 - 40$ km s^{-1}, respectively). Degenerate solutions include models with moderate velocities of 20 km s^{-1} and slightly higher densities of $10^{4.5}$ cm^{-3}. Best-fitting models are indicative of conditions very similar to those from the CO comparisons, for the warm gas, however for filling factors ~10 times lower.

The FPDF'10 C-type grid provides a larger set of lines for comparison (lower center panel of Fig. 19); however even best

Table 8. Comparison of molecular emission with shock models.

Model	Shock	Molecule	Component	v_s (km s^{-1})	n (cm^{-3})	b_{ff}
KN'96	C	H_2	"warm"	15	$10^{6.5}$	0.001 - 0.02
KN'96	C	H_2	"hot"	20	$10^{5.0} - 10^{5.5}$	0.003 - 0.03
FPDF'10	C	H_2	"warm"	10	$2 \times 10^{4.0}$	0.14 - 0.35
FPDF'10	C	H_2	"hot"	20	$2 \times 10^{4.0}$	0.01 - 0.09
FPDF'10	J	H_2	"'warm & hot"	20 - 30	$2 \times 10^{4.0}$	0.32 - 0.90
KN'96	C	CO	"warm"	30 - 35	$10^{4.5}$	0.10 - 0.24
KN'96	C	CO	"hot"	20 - 40	$10^{5.0} - 10^{6.5}$	0.001 - 0.03
FPDF'10[a]	C	CO	"warm"	40	$2 \times 10^{5.0}$	0.09 - 0.19
FPDF'10	J	CO	"warm & hot"	20	$2 \times 10^{4.0}$	0.50 - 0.98
KN'96	C	H_2O	"cold"	10 - 40	$10^{4.0} - 10^{5.0}$	0.05 - 0.21
FPDF'10	C	H_2O	"cold"	10 - 20	$2 \times 10^{4.0} - 2 \times 10^{5.0}$	0.17 - 0.46
FPDF'10	J	H_2O	"cold"	30	$2 \times 10^{5.0}$	0.01 - 0.1

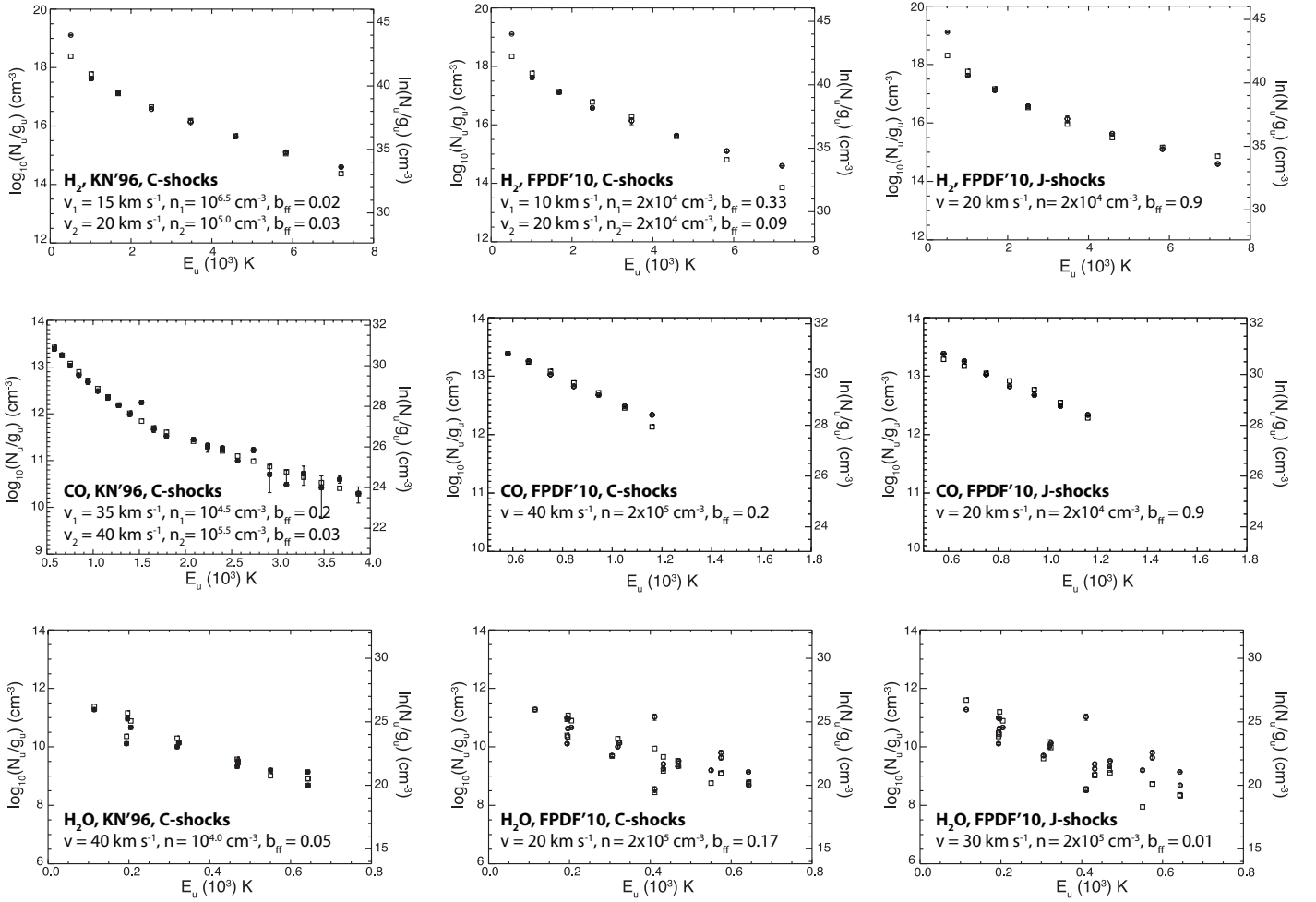[a] Comparison limited to $J_{up} = 20$ due to available model predictions

Fig. 19. Comparison between observed and best-fitting model intensities for H_2, CO and H_2O (top, middle and lower panels, respectively) displayed in excitation diagrams. C-type shock models from KN'96 and FPDF'10 are presented in the top and center columns, and J-type shocks from FPDF'10 in the right column. Best fitting model parameters are reported on each panel.

matching models do not reproduce sufficiently the observed lines in the high-energy regime. The solutions provided are highly degenerate and exclude only the highest density and velocity provided in the grid (40 km s^{-1} and 2×10^5 cm^{-3}). J-type shock comparisons (lower right panel of Fig. 19) do not reproduce the observations, and show a much larger scatter than the C-type shocks.

The OH/H_2O ratio can be used as indicator of the shock type, as shock models show that it varies from 10^{-2} in C-shocks (e.g. Kaufman & Neufeld 1996) to 10^2 in the high-velocity J-shocks (e.g. Neufeld & Dalgarno 1989). The low-velocity J-shock models of Flower et al. do not give predictions for OH, however it is reasonable to expect that the OH/H_2O ratio would be lower in these type of shocks. Even though the H_2O and OH column densities measured here are rather rough estimates, the large vari-

ation of their ratio predicted in extreme limits of shock conditions allows us to use them as a possible indicator. Assuming that emission from both molecules arises within the same volume of gas at the positions of peak emission, the OH/H_2O ratio is ~0.1. This is in favor of a C-type shock but only to the lowest limit of velocities estimated from the KN'96 models. The best fit solutions for the majority of the peaks indicate higher shock velocities, where the OH/H_2O ratio is expected to be < 0.01. The OH line flux at 119.23 μm agrees with the predictions of Kaufman & Neufeld (1996) for the densities and velocities derived for H_2O in C-shocks. In contrast, the sum of fluxes over all OH lines in the PACS range is more than an order of magnitude lower than the values predicted for J-shocks (Hollenbach & McKee 1989), even if scaled for the corresponding range of filling factors. In conclusion, shock models and line ratios suggest that the H_2O and OH emission is likely to arise in C-type shocks.

4.2.3. Atomic emission

Oxygen in shocks is produced in large amounts through sputtering from dust grains and dissociation of molecules. The efficiency of this process depends largely on the shock velocity and shock type (Hollenbach & McKee 1989). Models predict high abundances especially of the $^3P_1$-$^3P_2$ [OI] line at 63μm in the case of dissociative J-type shocks; to test this, a number of diagnostic line ratios have been proposed (Hollenbach & McKee 1989; Flower & Pineau des Forêts 2010). The shock origin of the 63μm oxygen line is suggested here from its spatial distribution and close correlation to the outflows (see Sect. 3). Therefore, the [OI] emission provides a unique probe of the occurrence of J-type shocks.

Hollenbach & McKee (1989) proposed that the [OI](63μm)/[CII](158μm) intensity ratio would be expected to be below 10 if the emission is attributed to a photon-dominated region, and greater than 10 for J-type shocks. This is due partly to the high post-shock densities and temperatures, which favor [OI] production and partly by the rapid conversion of [CII] to CO in the high temperature post-shock chemistry which suppresses the [CII] emission. In the data presented here, the [OI](63μm)/[CII](158μm) ratio is >20 in the brightest regions (SMM3b and SMM4b), and drops to about 7 at SMM3r (see Table 1). This suggests that SMM3r is likely more affected by the diffuse [CII] emission from SMM6 (see Fig. 12).

The model grid of Flower & Pineau des Forêts (2010) includes predictions for the [OI] lines at both 63μm and 145μm. Figure 20 shows model-predicted line intensities against shock velocities; for the two densities taken into account in the model grid, [OI] model intensities define a locus for each shock-type. On the same figure, shaded areas defined by the minimum and maximum observed intensities are not corrected for beam filling factors and therefore represent lower limits in the case the emission is more compact. They stand well above the C-shock locus and define a common area with the J-type shocks, constraining for the given densities the shock velocity between 15-25 km s^{-1}, which agrees well with the velocity found for the best-fitting J-type shocks in the case of H_2 and CO. Correcting the observed intensities for the emitting region would result in higher shock velocities by ~ 5 km s^{-1}.

As pointed out by Flower & Pineau des Forêts (2010) collisional dissociation of H_2 in J-type shocks leads to the chemical dissociation through reactions with atomic hydrogen of H_2O, OH, O_2 and even CO which become rapid only at high kinetic temperatures reached by J-type shocks. As a diagnostic to the
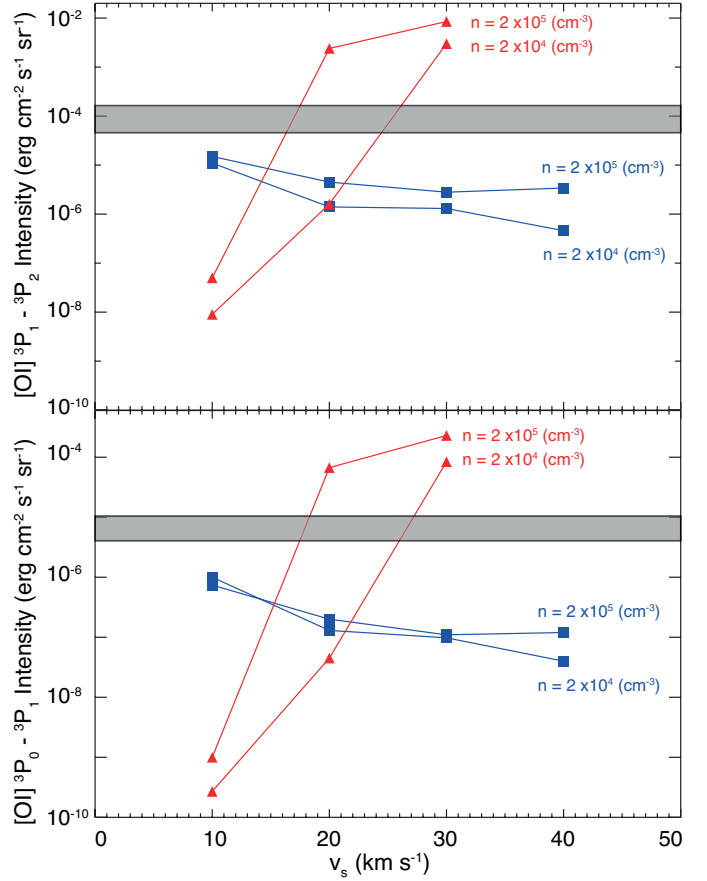

Fig. 20. [OI] line intensities for the $^3P_1$ - $^3P_2$ and the $^3P_0$ - $^3P_1$ transitions (*upper* and *lower* panels, respectively) versus shock velocity, for C- (blue) and J-type shocks (red) from FPDF'10 . The shaded area indicates the observed upper and lower line intensity limits. Observed intensities intercept only the J-shock predictions, constraining the shock velocities to 15-25 km s^{-1}.

shock type, Flower & Pineau des Forêts (2010) suggest accordingly the $[OI]/H_2$ ratio which tends to increase monotonically with the shock velocity for J-type shocks, but to decrease for C-type ones, assuming that H_2 and [OI] are co-existent. Figure 21 is a reproduction of Fig. 7 of Flower & Pineau des Forêts (2010) showing the [OI] over H_2 S(1) and S(3) line ratio predictions for a set of C and J shocks with the corresponding minimum and maximum values for the observed ratios overlaid. As suggested, the observed line ratio is consistent only with J-type shocks, at velocities of ~ 20-25 km s^{-1} for densities between 2×10^4 and 2×10^5 cm^{-3}.

The existence of dissociative shocks is also supported by the detection of [SI] at 25.2 μm, [FeII] at 26 μm and the enhancement of [SiII] at 34.8 μm at positions coincident with the [OI] peaks. Estimates from Hollenbach & McKee (1989) for J-shocks of u_s ~ 30 km s^{-1} and $n = 10^4$ cm^3 show that [SI], [FeII], [SiII] and [OI] at 145 μm lines have similar intensities between 1 and 4 ×10^{-4} erg cm^{-2} s^{-1} sr^{-1}, while the [OI] line at 63 μm is more than an order of magnitude brighter (~ 7 × 10^{-3} erg cm^{-2} s^{-1} sr^{-1}) and [CII] is negligible. These results reproduce accurately the measured line fluxes at the peak positions reported in Tables 1 and 2, for a beam ranging between 10 – 20% of the PACS spaxel size.
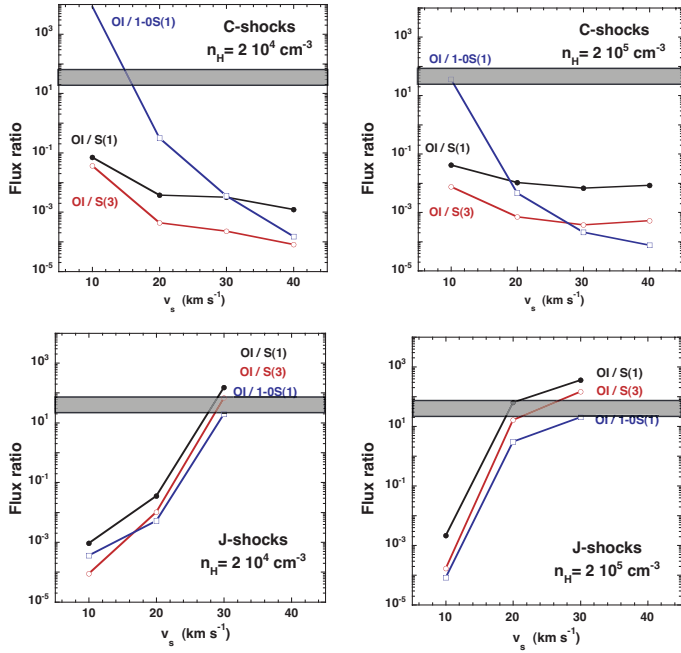
Fig. 21. Ratios of the [OI] $^3P_1$ - $^3P_2$ over the H_2 S(1) and S(3) lines, for pre-shock densities of 2×10^4 and 2×10^5 cm^{-3} (left and right panels, respectively) and C- or J-type shocks (upper and lower panels). Shaded areas show the observed upper and lower limits of the ratio for both H_2 transitions. The observed ratio overlaps only with J-shock model predictions, for velocities between 20-25 km s^{-1}. (*Figure adopted from FPDF'10*)

5. Discussion

Ample evidence for the occurrence of J-type shocks is provided by a number of different diagnostics. The high [OI] flux and the [OI]/H_2 and [OI]/[CII] ratios when confronted with models can only be interpreted by J-shocks. In addition, the relative flux levels of [FeII], [SiII], [SI], and the two [OI] lines are consistent with the J-type shock predictions of (Hollenbach & McKee 1989). Further evidence stems from the comparisons of the H_2 and CO emission (the latter for $J_{up} \leq 20$) in a single-shock scheme. All diagnostics converge to a common set of values with velocities ranging from 20 to 30 km s^{-1}, pre-shock densities between 10^4 and 10^5 cm^{-3}, and beam filling factors of $10 - 90\%$. To the upper limit, such filling factors are hard to interpret, however they may occur when comparing a projected 3-D bow-shock structure on the plane of the sky with 1-D model data.

C- type shocks are suggested from the comparisons with the emission from water, the OH/H_2O ratio and the low OH flux levels. C-shocks can reproduce the emission from CO and H_2, however in a piecewise fashion with two shock components corresponding to the "warm" and "hot" gas. The warm gas emission from CO and H_2 along with H_2O can be reproduced by models with high velocities ($30 - 40$ km s^{-1}) and low-to-intermediate densities (10^4 - 10^5 cm^{-3}). For the hot gas, predicted shock conditions vary significantly between different molecules so that it is difficult to define a common set of solutions. Beam filling factors vary between 0.1% and 30% for the "hot" and "warm" gas. The scatter in the shock conditions can be interpreted as the emission originating from a projected, two-dimensional bow-shock. In this scenario, higher excitation lines would originate from a higher temperature gas closer to the bow-head, where compression is higher and therefore filling factors are low. In a similar fashion, lower excitation lines would originate from

the bow-shock wings where compression is lower and thus filling factors higher. The two-dimensional bow-shock scenario can also accommodate the large span in shock velocities and densities retrieved from model comparisons for different molecules. J-shocks cannot fit this picture though, as in contrast to the values derived here beam filling factors would need to be smaller than C-shocks. Such a scenario could be reconciled with a non-steady, truncated C-shock with an embedded magnetic precursor (C+J shocks). However such models were not available for comparisons.

In a recent study, Benedettini et al. (2012) demonstrated that the [OI], OH and CO emission traced with PACS in the B1 region on the outflow of L1157 is consistent only with dissociative J-shocks. It is worth noticing that the [OI] levels in L1157 are similar to the ones observed here, however CO is only detected up to $J_{up} = 22$. Therefore at least the atomic lines here and in the study of Benedettini et al. (2012) provide strong indications for the existence of J-type shocks. Another study focusing on HH54 (Bjerkeli et al. 2011), concludes that the observed cooling rates between CO and water can only be reconciled if J-shocks are taken into account. Concerning the molecular lines, a similar comparison of rotational H_2 emission in the protostellar outflow from HH211 (Dionatos et al. 2010b) has provided consistent results with the current study. C- and J-type shocks can account for the observed line intensities considering low and high beam filling factors, respectively. Comparisons of CO and H_2 emissions from ISO and ground based facilities in the case of HH54 (Giannini et al. 2006) have concluded that C-type shocks are not sufficient to reproduce the observed intensities from both molecules. Giannini et al. (2006) find that a steady state J-type or a quasi-steady J-type shock with a magnetic precursor (C+J shock) can best fit the observed line intensities. More recently, water emission observed with HIFI (Santangelo et al. 2012) was suggested to originate in J-shocks, which is not consistent with the findings from the shock model comparisons above. However, Kristensen et al. (2012) has shown that the water line profiles resolved with HIFI are complex, tracing simultaneously more than one processes.

Mechanisms other than shocks may be responsible for the excitation of gas. Visser et al. (2012) have demonstrated that CO emission in the PACS range can be reproduced partly by UV heating of the envelope gas and partly by C- shocks acting on the outflow cavity walls. Around SMM3 and SMM4, the bulk of [CII] emission is associated with SMM6, however some [CII] emission is also observed along the outflows. A protostellar source with UV luminosity of ~ 0.1 L$_\odot$, as indicated by best-fitting model-sources of Visser et al. (2012) would give an unattenuated UV flux of ~ 10 G_0 at a distance of 4000 AU from the source (e.g. the distance of the outflow positions from SMM3). Adopting an envelope density of $\sim 10^4$ cm^{-3} as found in Visser et al. (2012), and using the PDR model of Kaufman et al. (1999) we find [CII] flux levels of $\sim 10^{-14}$ erg cm^{-2} s^{-1} within the area of a PACS spaxel. This estimate corresponds well to the values reported in Table 1 ($0.5 - 2.5$ $\times 10^{-14}$ erg cm^{-2} s^{-1}). However, in this scenario where the envelope gas is heated by UV radiation from the protostar, the [CII] flux should drop as a function of distance from the exciting source. As reported in Table 1, the [CII] flux levels at the outflow peaks are ~4 times higher than the spaxel closest to the source (SMM3c), Therefore the gas excitation due to UV radiation from the protostar is not consistent with the distribution of the [CII] flux demonstrated by the current data. If [CII] excitation is attributed mostly to SMM6, then lower UV levels from

SMM3 would play a minor role in the gas excitation at the distances examined.

The analysis in Sect. 3 and Sect. 4 suggests a common origin for the H_2 and CO emission. The observed two-temperature component may be interpreted by either two component C- or single component J-type shocks. The difference by a factor between 3 and 10 in CO/H_2 ratio measured for the warm and hot gas components cannot be easily interpreted by a C-shock chemistry, as such shocks are non-dissociative and therefore the abundances of major molecular gas constituents are not expected to change significantly. In addition, sputtering of ice mantles from the dust grains is a very efficient process in C-shocks with velocities greater than ~ 15 km s^{-1}, due to the differential speed between the neutral and the charged fluids. Therefore C-shocks cannot easily interpret the observed variation in the CO/H_2 ratio, either through chemical reactions or depletion through the formation of ices onto dust grains.

The H_2 binding energy is almost 3 times lower than that of CO; therefore dissociative J-shocks should in principle have a more destructive impact on H_2 rather than CO molecules. Once H_2 is dissociated though, CO can be efficiently dissociated in chemical reactions with atomic hydrogen (Hollenbach & McKee 1989). Therefore in a fully dissociative shock, both CO ands H_2 emission would originate in the post-shock gas, when temperatures drop enough to allow molecules to reform. H_2 reformation occurs on dust grains, and therefore the efficiency of H_2 production depends on the survival of dust in the post-shock gas. On the other hand, CO can be produced rapidly through fast-neutral reactions in the gas phase, as long as the temperature remains higher than 300 K (see Fig.2 in Hollenbach & McKee 1989). As the post-shock gas cools down CO reforms and is eventually adsorbed onto dust grains, where H_2 is produced and ejected into the gas phase (Flower & Pineau des Forêts 2010). In this scheme, J-type shocks can explain the CO abundance variation; CO is more abundant in the hot gas where H_2 is still partially dissociated and CO forms through fast gas-phase reactions. The warm gas abundance ratio is then consistent with the CO being adsorbed and the H_2 desorbed from/onto dust grains as the gas cools down. The J-shock scenario seems to provide explanation to the CO abundance variation, however there are two caveats. First, CO dissociation is expected to produce strong [CI] emission which is not observed on the outflows in APEX/CHAMP+ maps of Serperns (L E. Kristensen, in prep.). Furthermore, the shock conditions and beam filling factors reported in Table 8 for H_2 and CO are essentially identical, which may indicate intrinsic weaknesses of the comparisons and the model solutions.

In a different scenario, the hot and warm gas emission may represent cooling due to J- and C-type shocks, respectively. As mentioned in Sect. 3, the temperature break in H_2 and CO is observed in a large number of outflows, and is likely to reflect an omnipresent phenomenon related to the underlying physical processes. To test this, a larger sample of protostellar outflows and more detailed shock models are necessary.

6. Conclusions

We have carried out spectro-imaging observations of SMM3 and SMM4 in Serpens with Herschel/PACS and Spitzer/IRS. These observations provide an almost complete wavelength coverage from 5 μm to 190 μm, at angular resolutions of $\sim 9.4''$ and reveal a wealth of lines originating from rotational transitions of H_2, CO, H_2O, OH, as well as forbidden transitions of [OI], [CII],

[FeII], [SI] and [SiII]. The main results are summarized as follows:

– The morphology of molecular (H_2, CO, H_2O and OH) and atomic emission ([OI], [FeII], [SiII], [SI]) line maps observed with Herschel/PACS and Spitzer/IRS is consistent with the excitation of these species in outflows. The only exception is the emission from [CII], which is likely to be excited by UV radiation from the nearby protostellar source SMM6.

– Line emission in SMM3 is extended, following an SE-NW outflow pattern. For SMM4, line emission shows one significant peak at $\sim 10''$ to the N-NW from the protostar.

– CO and H_2 trace gas at temperatures of ~ 300 and ~ 1000 K. Within the available resolution, emission from both molecules is confined to the same areas along outflows, and their emission pattern has very similar morphological characteristics. These findings suggest that CO and H_2 are excited by a common underlying mechanism.

– H_2O and OH trace gas at rotational temperatures in the range ~ 100-200 K. Even though these species are chemically related, the large scatter of data points in the excitation analysis does not allow us to tightly constrain their properties.

– The association between CO and H_2 allows us to directly estimate the CO abundance in excited gas. The CO/H_2 ratio is found to vary from 10^{-5} at ~ 300 K up to 2×10^{-4} at ~ 1000 K.

– The existence of dissociative J-type shocks is strongly suggested by the high atomic line fluxes as well as diagnostics of the $[OI]/H_2$ ratio. In addition J-shocks can reproduce the observed H_2 emission and the CO emission at ~ 300 K. The lack of model predictions for $J_{up} \geq 20$ prevents a conclusive test of whether J-shocks can reproduce the warm gas traced by CO. All J-shock diagnostics and model comparisons provide consistent pre-shock densities of 2×10^4 cm^{-3}, shock velocities from 15 to 25 km $^{-1}$ and beam filling factors from 10% to 90%. This common set of shock parameters is consistent with a common physical mechanism responsible for the excitation of CO and H_2. J-shock models however, cannot sufficiently reproduce the observed H_2O emission.

– C-shocks can reproduce the observed emission for CO and H_2 only if two temperatures and small beam filling factors are considered, suggesting a layered temperature structure, possibly in a bow-shock. Non-dissociative shocks fit best the H_2O emission. The predicted pre-shock densities and velocities vary significantly for different species, in support of a projected 2-dimensional layering.

– The two-temperature structure for CO and H_2 has been observed in the majority of outflows from protostellar sources. The current analysis indicates that this structure is likely to reflect a physical break between C- and J-type shocks.

The physical association between CO and H_2 indicated here, needs to be also confirmed in different protostellar environments. DIGIT embedded sources that have been mapped with Spitzer will be analyzed in a follow-up paper. If this association is more general, then this larger sample will help to better constrain the ratio between CO and H_2 in the warm gas around young protostars. In addition, more complete and detailed shock models are required in order to control the influence of different types of shocks on the abundances of both molecules.

References

Arce, H. G., Shepherd, D., Gueth, F., et al. 2007, Protostars and Planets V, 245

Benedettini, M., Busquet, G., Lefloch, B., et al. 2012, A&A, 539, L3

Bjerkeli, P., Liseau, R., Nisini, B., et al. 2011, A&A, 533, A80

Davis, C. J., Matthews, H. E., Ray, T. P., Dent, W. R. F., & Richer, J. S. 1999, MNRAS, 309, 141

Dedes, C., Röllig, M., Mookerjea, B., et al. 2010, A&A, 521, L24

Dionatos, O., Nisini, B., Cabrit, S., Kristensen, L., & Pineau Des Forêts, G. 2010a, A&A, 521, A7

Dionatos, O., Nisini, B., Codella, C., & Giannini, T. 2010b, A&A, 523, A29

Dzib, S., Loinard, L., Mioduszewski, A. J., et al. 2010, ApJ, 718, 610

Eiroa, C., Palacios, J., Eisloffel, J., Casali, M. M., & Curiel, S. 1997, in IAU Symposium, Vol. 182, Herbig-Haro Flows and the Birth of Stars, ed. B. Reipurth & C. Bertout, 103P

Enoch, M. L., Glenn, J., Evans, II, N. J., et al. 2007, ApJ, 666, 982

Evans, II, N. J., Allen, L. E., Blake, G. A., et al. 2003, PASP, 115, 965

Evans, II, N. J., Dunham, M. M., Jørgensen, J. K., et al. 2009, ApJS, 181, 321

Flower, D. R. & Pineau des Forêts, G. 2010, MNRAS, 406, 1745

Giannini, T., McCoey, C., Nisini, B., et al. 2006, A&A, 459, 821

Giannini, T., Nisini, B., & Lorenzetti, D. 2001, in Astronomical Society of the Pacific Conference Series, Vol. 243, From Darkness to Light: Origin and Evolution of Young Stellar Clusters, ed. T. Montmerle & P. André, 341

Goicoechea, J. R., Cernicharo, J., Karska, A., et al. 2012, A&A, 548, A77

Goldsmith, P. F. & Langer, W. D. 1999, ApJ, 517, 209

Graves, S. F., Richer, J. S., Buckle, J. V., et al. 2010, MNRAS, 409, 1412

Green, J. D., Evans, II, N. J., Jørgensen, J. K., et al. 2013, ArXiv e-prints

Haisch, Jr., K. E., Barsony, M., Greene, T. P., & Ressler, M. E. 2002, AJ, 124, 2841

Harvey, P., Merín, B., Huard, T. L., et al. 2007, ApJ, 663, 1149

Herbst, T. M., Beckwith, S. V. W., & Robberto, M. 1997, ApJ, 486, L59

Herczeg, G. J., Karska, A., Bruderer, S., et al. 2012, A&A, 540, A84

Högbom, J. A. 1974, A&AS, 15, 417

Hogerheijde, M. R., van Dishoeck, E. F., Salverda, J. M., & Blake, G. A. 1999, ApJ, 513, 350

Hollenbach, D. & McKee, C. F. 1989, ApJ, 342, 306

Houck, J. R., Roellig, T. L., van Cleve, J., et al. 2004, ApJS, 154, 18

Karska, A., Herczeg, G. J., van Dishoeck, E. F., et al. 2013, A&A, 552, A141

Kaufman, M. J. & Neufeld, D. A. 1996, ApJ, 456, 611

Kaufman, M. J., Wolfire, M. G., Hollenbach, D. J., & Luhman, M. L. 1999, ApJ, 527, 795

Kessler, M. F., Steinz, J. A., Anderegg, M. E., et al. 1996, A&A, 315, L27

Kristensen, L. E., van Dishoeck, E. F., Bergin, E. A., et al. 2012, ArXiv e-prints

Kristensen, L. E., van Dishoeck, E. F., van Kempen, T. A., et al. 2010a, A&A, 516, A57

Kristensen, L. E., Visser, R., van Dishoeck, E. F., et al. 2010b, A&A, 521, L30

Lacy, J. H., Knacke, R., Geballe, T. R., & Tokunaga, A. T. 1994, ApJ, 428, L69

Lahuis, F., van Dishoeck, E. F., Jørgensen, J. K., Blake, G. A., & Evans, N. J. 2010, A&A, 519, A3

Larsson, B., Liseau, R., & Men'shchikov, A. B. 2002, A&A, 386, 1055

Larsson, B., Liseau, R., Men'shchikov, A. B., et al. 2000, A&A, 363, 253

Lindberg, J. E. & the DIGIT team. 2013, A&A, in prep.

Maret, S., Bergin, E. A., Neufeld, D. A., et al. 2009, ApJ, 698, 1244

Müller, H. S. P., Schlöder, F., Stutzki, J., & Winnewisser, G. 2005, Journal of Molecular Structure, 742, 215

Narayanan, G., Moriarty-Schieven, G., Walker, C. K., & Butner, H. M. 2002, ApJ, 565, 319

Neufeld, D. A. 2012, ApJ, 749, 125

Neufeld, D. A. & Dalgarno, A. 1989, ApJ, 340, 869

Neufeld, D. A., Melnick, G. J., Sonnentrucker, P., et al. 2006, ApJ, 649, 816

Neufeld, D. A., Nisini, B., Giannini, T., et al. 2009, ApJ, 706, 170

Nisini, B., Benedettini, M., Giannini, T., et al. 2000, A&A, 360, 297

Nisini, B., Giannini, T., Neufeld, D. A., et al. 2010, ApJ, 724, 69

Pickett, H. M., Poynter, R. L., Cohen, E. A., et al. 1998, J. Quant. Spec. Radiat. Transf., 60, 883

Pilbratt, G. L., Riedinger, J. R., Passvogel, T., et al. 2010, A&A, 518, L1

Poglitsch, A., Waelkens, C., Geis, N., et al. 2010, A&A, 518, L2

Preibisch, T. 2003, A&A, 410, 951

Rieke, G. H. & Lebofsky, M. J. 1985, ApJ, 288, 618

Santangelo, G., Nisini, B., Giannini, T., et al. 2012, A&A, 538, A45

Sheffer, Y., Rogers, M., Federman, S. R., et al. 2008, ApJ, 687, 1075

Smith, J. D. T., Armus, L., Dale, D. A., et al. 2007, PASP, 119, 1133

Straižys, V., Černis, K., & Bartašiūtė, S. 2003, A&A, 405, 585

Strom, S. E., Vrba, F. J., & Strom, K. M. 1976, AJ, 81, 638

Testi, L., Sargent, A. I., Olmi, L., & Onello, J. S. 2000, ApJ, 540, L53

van Dishoeck, E. F. 2004, ARA&A, 42, 119

van Dishoeck, E. F. & Black, J. H. 1987, in NATO ASIC Proc. 210: Physical Processes in Interstellar Clouds, ed. G. E. Morfill & M. Scholer, 241–274

van Dishoeck, E. F., Glassgold, A. E., Guelin, M., et al. 1992, in IAU Symposium, Vol. 150, Astrochemistry of Cosmic Phenomena, ed. P. D. Singh, 285

van Kempen, T. A., Kristensen, L. E., Herczeg, G. J., et al. 2010, A&A, 518, L121

Visser, R., Kristensen, L. E., Bruderer, S., et al. 2012, A&A, 537, A55

Wampfler, S. & the WISH team. 2012, A&A, submitted

Watson, D. M., Genzel, R., Townes, C. H., & Storey, J. W. V. 1985, ApJ, 298, 316

Werner, M. W., Roellig, T. L., Low, F. J., et al. 2004, ApJS, 154, 1

Wilgenbus, D., Cabrit, S., Pineau des Forêts, G., & Flower, D. R. 2000, A&A, 356, 1010

Winston, E., Megeath, S. T., Wolk, S. J., et al. 2007, ApJ, 669, 493

Appendix A: Spitzer spectral line maps of Serpens SE

Spitzer/IRS maps at their full extent and resolution. Maps of the pure rotational H_2 lines S(2) - S(7) falling in the SL module wavelength range are presented in figure A.1. For reference, the positions of SMM3 and SMM4 are indicated with filled orange circles. In order to obtain maximum coverage, both on and off positions were used for the compilation of the SL1 and SL2 module data-cubes. This extended coverage appears to the N or the S (SL2 and SL1 modules, respectively) of SMM3 and SMM4. The resolution of the SL maps is 3.5″ per spaxel, and weak emission-like stripes are due to residual rogue pixels during the reduction. Figure A.2 presents the S(1), S(0) H_2 line maps, along with ones corresponding to atomic lines from [SI], [FeII] and [SiII] (at 25.2, 26.0 and 34.8 μm). The LL map resolution is 10.5″ per spaxel.

Appendix B: Short description of the POMAC code

The POMAC (Poor-man's CLEAN) algorithm (Lindberg et al., in prep.) is a deconvolution algorithm used to separate point sources from extended emission in PACS data. The code is a modified version of the CLEAN algorithm (Hgbom 1974), with the difference that it requires the positions of testing "point" sources. Such points in the present case are selected to be the spaxels displaying emission maxima. The code produces instrument PSFs corresponding to point sources in each pre-defined point source position for the wavelength of the spectral line (or continuum emission) that is to be deconvolved. This is constructed by assuming the Herschel telescope primary beam to be a Rayleigh-criterion Gaussian, which is then overlaid on the PACS spaxel grid to measure how much of the Gaussian that falls into each spaxel.

After the PSFs have been determined, the CLEAN part of the code commences. It studies the line (or continuum) emission in the PACS grid to find the pre-defined point source responsible for the strongest flux in the field. A fraction of this flux convolved with the PSF of that point source is subtracted from the line map, and the subtracted flux is added to the cleaned flux of this point source. This step is then repeated until certain stop criteria are met. The remaining flux in the residual map is then composed of extended emission and emission from any unknown point sources, and the cleaned line fluxes correspond
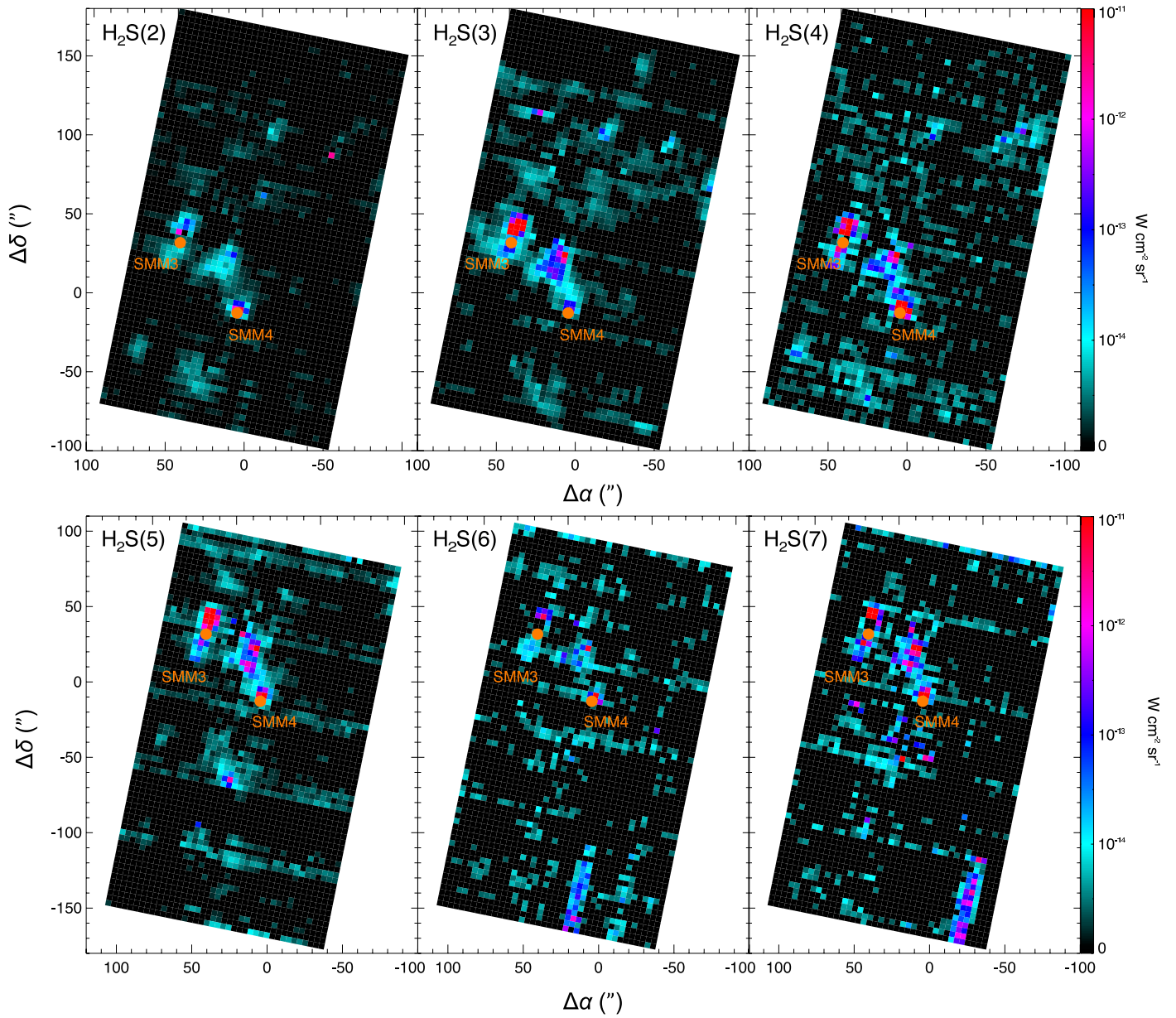
Fig. A.1. Spitzer/IRS H_2 maps obtained with the SL modules, at a resolution of $3.5''$/spaxel

to that of the point sources. Note that the residual map is non-deconvolved, and shall not be interpreted as a deconvolved map of the extended emission. Finally, the sum of the cleaned flux and the residual flux is compared to the original map as a consistency check. For a well-centered point source without extended emission (such as the continuum emission of HD100546) the results of this method agree well with the results from the PSF correction factor method (the differences are less than 20% across the PACS band).
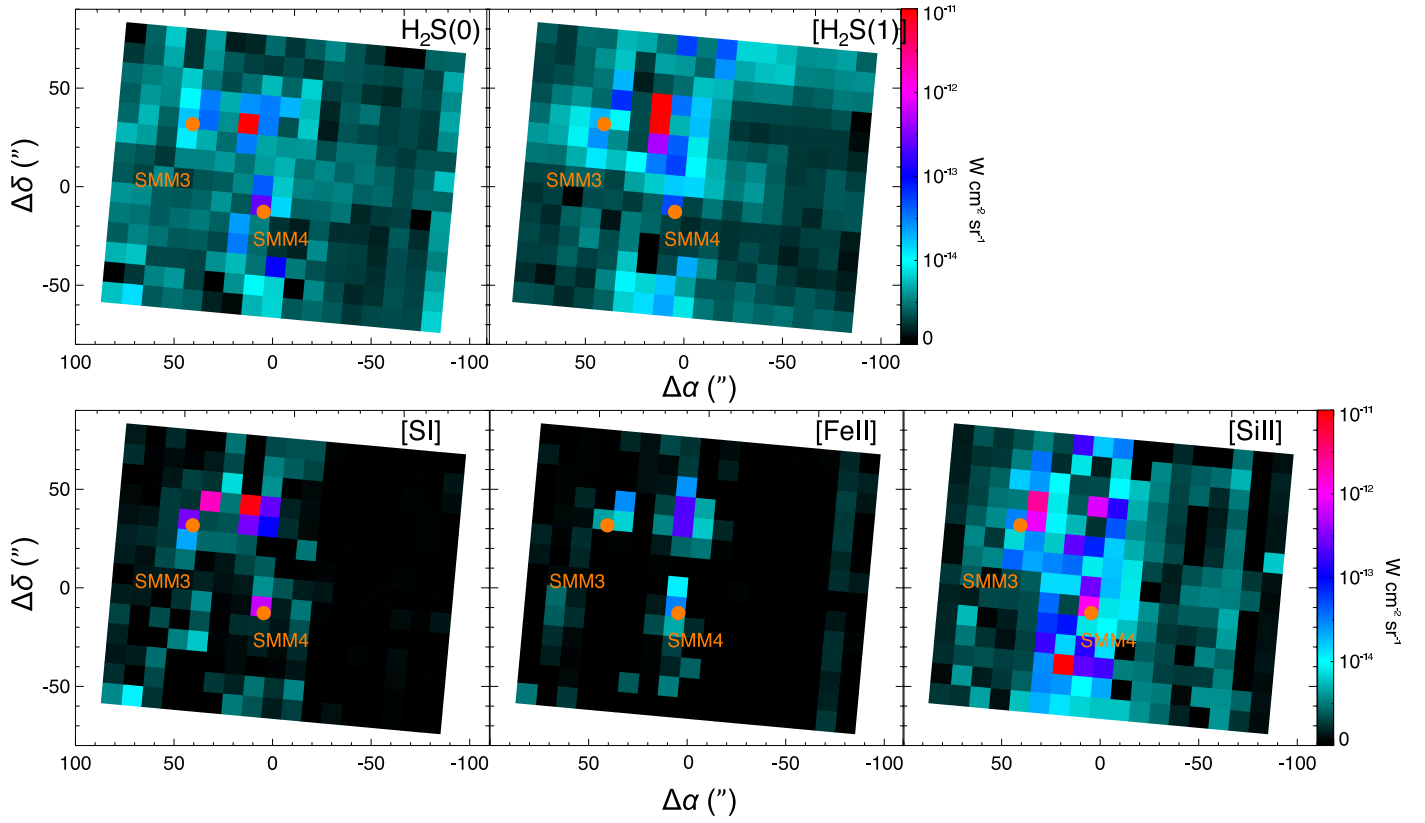
Appendix C: Excitation diagrams

Fig. A.2. Spitzer/IRS line maps of the S(0)l and S(1) H_2 transitions, along with atomic line maps from the LL modules at a resolution of 10.5″/spaxel

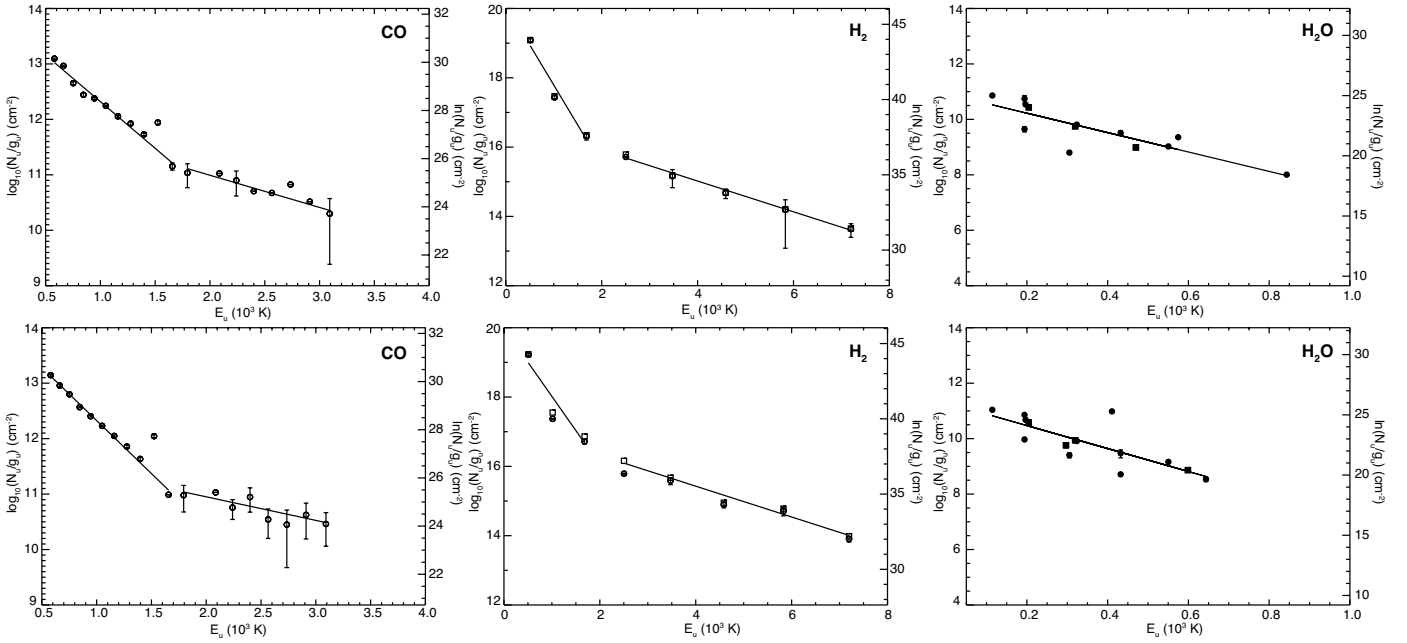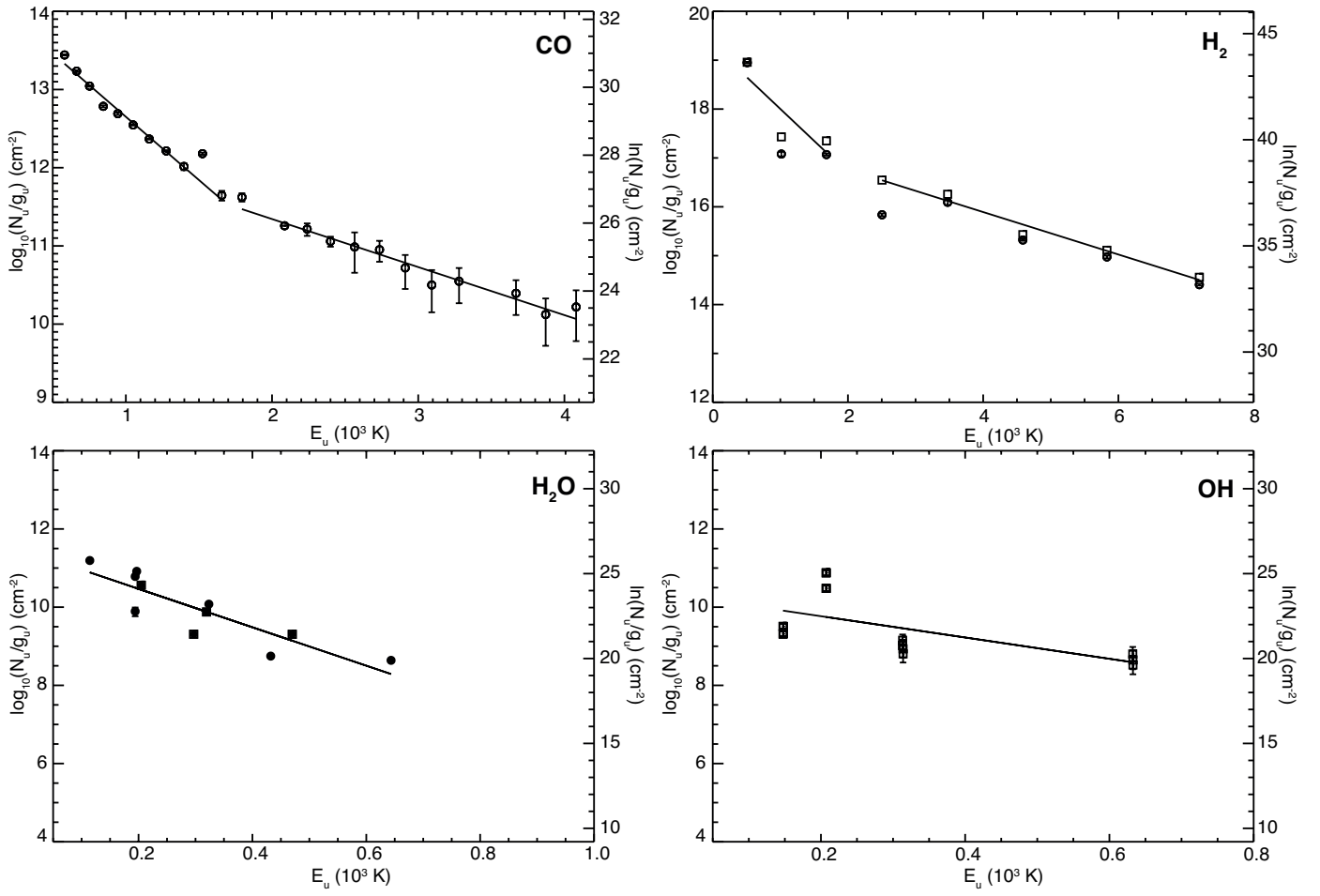**Fig. C.1.** Excitation diagrams for CO, H_2 and H_2O at SMM3c and SMM3r (upper and lower panels, respectively)

Fig. C.2. Excitation diagrams for CO, H_2, H_2O and OH at SMM4c